

AN ABSTRACT OF THE THESIS OF

Hailey Bond for the degree of Master of Science in Civil Engineering presented on September 10, 2020.

Title: Beach Dune Subsurface Hydrodynamics and the Formation of Dune Scarps.

Abstract approved:

Meagan E. Wengrove

The formation of beach scarps is a challenging morphodynamic phenomenon that the coastal community has yet to capture in coastal change models. Understanding scarp formation is crucial to accurately predicting coastal erosion and vulnerability during extreme events, as models without parameters for scarp formation and development severely underpredict total erosion volumes. In models, the transition from planar beach slope to scarp is triggered by the exceedance of an empirical user-defined beach slope. However, little is known about the subsurface physical processes that can precipitate the formation of these highly erosive features.

Our work presents results from a near-prototype experiment undertaken to examine both the subsurface and subaerial hydrodynamics involved in the erosion of a beach dune under hurricane conditions. Data was collected during a scaled simulation of Hurricane Sandy on a 1:2.5 scale beach dune in the NSF NHERI O.H. Hinsdale Wave Research Laboratory Large Wave Flume. Pressure and moisture sensors ($f = 100$ Hz) buried within the dune tracked the location of the water table over the course of the experiment and captured the influence of wave runup events on pore water pressure and moisture content within the dune. A line-scan lidar ($f = 2$ Hz) determined the runup elevation of each bore and tracked erosion along a single cross-shore transect throughout the experiment.

During the experiment, a vertical scarp formed on the beach face as the water level and wave height increased. Throughout the period of scarp formation, a local increase in the total hydraulic head developed underneath the swash zone. Moisture sensors confirm that the sand in the swash zone was saturated, which indicates a reduction in matric suction from the

partially saturated state. Partial momentary liquefaction events, which destabilize surficial sediments on the beach face, were also observed as the scarp forms. Partial momentary liquefaction events are positively correlated with both the total hydraulic head and the swash bore depth. While a reduction in matric suction and an increase in partial momentary liquefaction events can explain some of the slope steepening observed during the experiment, the initial slope discontinuity that developed into the scarp was observed prior to the occurrence of our observations of these instabilities.

©Copyright by Hailey Bond
September 10, 2020
All Rights Reserved

Beach Dune Subsurface Hydrodynamics and the Formation of Dune Scarps

by
Hailey Bond

A THESIS

submitted to

Oregon State University

in partial fulfillment of
the requirements for the
degree of

Master of Science

Presented September 10, 2020
Commencement June 2021

Master of Science thesis of Hailey Bond presented on September 10, 2020

APPROVED:

Major Professor, representing Civil Engineering

Head of the School of Civil and Construction Engineering

Dean of the Graduate School

I understand that my thesis will become part of the permanent collection of Oregon State University libraries. My signature below authorizes release of my thesis to any reader upon request.

Hailey Bond, Author

ACKNOWLEDGEMENTS

I would first like to thank my advisor, Meagan Wengrove, for her time, support, and insistent belief that I had what it took to be a researcher. You've pushed me to grow in ways I didn't think I was capable of. My two years at Oregon State have been more transformational professionally and personally than I could have imagined.

I would also like to express my appreciation to all the researchers I had the opportunity to work with in the wave lab during the summer of 2019. Your enthusiasm, energy, and hard work made our lab experiment truly a once-in-a-lifetime experience. Thank you to Tim Maddux, Pedro Lomónaco, and Brett Bosma for all your patience in teaching me to work everything from a crimper to the wavemaker and making me feel at home in the lab.

Many thanks go to Annika O'Dea for her help processing my lidar data, I would still be stuck in the weeds of lidar rectification if it wasn't for your help.

I am so thankful for the wonderful friends and roommates that I've had the privilege of getting to know over the last two years. You were all instrumental in helping me navigate the highs and lows of grad school. The adventures, dinner nights, and other assorted shenanigans are some of my favorite memories of grad school.

And finally, thanks as always to my family for their support as I muddle my way through life in the Pacific Northwest.

This material is based upon work supported by the National Science Foundation under Grant Nos. #1519679, #1520817, and #1756449.

TABLE OF CONTENTS

	<u>Page</u>
1. Introduction.....	1
1.1 Mechanisms of Process Driven Scarp Formation.....	1
1.1.1 Swash dynamics and runup	2
1.1.2 Goundwater levels and sediment suction	2
1.1.3 Partial momentary liquefaction	4
2. Methods.....	6
2.1 Experimental Setup	6
2.2 Instrumentation.....	7
2.3 Signal Processing	8
2.3.1 Moisture Sensors	8
2.3.2 Pressure sensors.....	8
2.2.3 Lidar	9
3. Results.....	11
3.1 Dune scarp morphological development	11
3.2 Dune interior pressure head.....	14
3.3 Dune sediment moisture content	15
3.4 Dune sediment partial momentary liquefaction.....	16
4. Discussion	20
5. Conclusion	26
6. References.....	29
Appendix A: Geotechnical Testing.....	31
Appendix B: Lidar Processing	39
Appendix C: Forcing Conditions	44

LIST OF FIGURES

<u>Figure</u>	<u>Page</u>
Figure 1: Diagram of the subsurface hydrodynamics in the swash zone, from Heiss (2015).....	3
Figure 2: Forcing conditions for experiment: (a) significant wave height, (b) wave period, and (c) water level. Red squares show the time period of scarp formation.....	7
Figure 3: A selection of instrument locations within the dune	8
Figure 4: Changes in the dune profile over the course of the experiment. Note that the intervals between presented profiles are uneven, as the dune eroded slowly at first and quickly at the end of the experiment.....	11
Figure 5: Photos of the dune as it eroded.....	12
Figure 6: Changes in the dune profile and interior dune water table during the period of scarp formation. Sensors referenced later are also included.	13
Figure 7: Changes in dune properties from trial 33 – 40: (a) time stack of erosion across profile in reference to the initial profile of trial 36, (b) time stack of slope, (c) average and maximum runup (d) changes in moisture content of sensors in the upper 30 cm of sand at meters 76, 77, and 78, and (e) excess pore pressure gradients between sensors P2 & P3 and between sensors P3 & P7, with negative gradients shaded in red.	14
Figure 8: A selection of 200 seconds of data from trial 36: (a) time stack of swash depth, with runup extent marked in red and the cross-shore location of sensors marked in orange, (b) time series of swash depth at location of sensors, (c) volumetric moisture content for sensors M14, M2, and M15, colored by their absolute moisture content, (d) excess pore pressure gradients between sensors P2 & P3 and between sensors P3 & P7, with negative gradients shaded in red.....	17
Figure 9: A selection of 200 seconds of data from trial 38: (a) time stack of swash depth, with runup extent marked in red and the cross-shore location of sensors marked in orange, (b) time series of swash depth at location of sensors, (c) volumetric moisture content for sensors M14, M2, and M15, colored by their absolute moisture content, (d) excess pore pressure gradients between sensors P2 & P3 and between sensors P3 & P7, with negative gradients shaded in red.....	18
Figure 10: A selection of 200 seconds of data from trial 40: (a) time stack of swash depth, with runup extent marked in red and the cross-shore location of sensors marked in orange, (b) time series of swash depth, (c) volumetric moisture content for sensors M14, M2, and M15, colored by their absolute moisture content, (d) excess	

pore pressure gradients between sensors P2 & P3 and between sensors P3 & P7, with negative gradients shaded in red. 19

Figure 11: (a) – (f): Correlation between SSE - THH, x-axis, swash depth (y-axis), and magnitude of partial momentary liquefaction events (color). (g) shows the progression of the scarp and the relative water table elevation throughout the trials displayed in (a) – (f)..... 22

Figure 12: A selection of 200 seconds of data from trial 38: (a) time stack of swash depth, with runup extent marked in red and the cross-shore location of sensors marked in orange, (b) volumetric moisture content for sensors M29 and M30, colored by their absolute moisture content , (c) volumetric moisture content for sensors M14, M2, and M15, colored by their absolute moisture content, (d) excess pore pressure gradients between sensors P2 & P3 and between sensors P3 & P7, with negative gradients shaded in red..... 25

LIST OF APPENDIX FIGURES

<u>Figure</u>	<u>Page</u>
Appendix A: Geotechnical Testing	
Figure 1: Results from the Modified Proctor compaction test.....	32
Figure 2: Results from grain size distribution test (courtesy of Pegah Ghasemi).....	33
Figure 3: Results from dynamic cone penetrometer field testing.....	34
Figure 4: Results from dynamic cone penetrometer test section testing.....	35
Figure 5: Results from dynamic cone penetrometer testing on the bare dune..	36
Figure 6: Moisture sensor calibration curves for all sensors tested.....	37
Figure 6: Moisture sensor calibration curves for all sensors tested (grey) and averaged curve (red).....	38
Appendix B: Lidar Processing	
Figure 1: Typical frame scan with reflectors and rectification planes.....	41
Figure 2: Data used to identify lidar time lag: (a) runup derived from dune-view camera, (b) runup derived from berm-view camera, (c) runup derived from lidar.....	43
Appendix C: Lidar Processing	
Figure 1: Hurricane Harvey storm surge.....	44
Figure 2: Hurricane Joaquin storm surge.....	44
Figure 3: Hurricane Michael storm surge.....	44
Figure 4: Hurricane Sandy storm surge.....	44

1. Introduction

Coastal dunes are an important protective feature of many sandy coasts around the world. During storms, dune systems are vulnerable to surge erosion and overtopping under elevated water levels and wave heights (Sallenger, 2000). As such, accurate prediction of coastal dune erosion is of critical importance for many low-lying areas susceptible to flooding. When beaches are in an erosive state, vertical discontinuities in the foreshore beach profile, called scarps, are a common occurrence (Sherman and Nordstrom, 1985). Scarps can form through process controls (eg. waves and currents), and through structural controls (eg. frozen beaches or beach vehicle tracks) (Sherman and Nordstrom, 1985).

We focus on beach dune scarp formation through process controls. Process controlled beach dune scarps are hypothesized to form in response to changes in hydrodynamic conditions, such as an increase in wave energy or change in the angle of wave approach toward the beach (Sherman and Nordstrom, 1985). Field studies note that changes in hydrodynamic conditions cause the beach profile to gradually steepen until slumping begins to occur (van Bemmelen et al., 2020).

After a scarp forms, the scarp enters the migration phase, where the scarp moves shoreward and generally becomes taller. During scarp migration, the mechanism for erosion is slumping and/or undercutting (Sherman and Nordstrom, 1985; van Bemmelen et al., 2020). Undercutting of a scarp occurs when the toe of the scarp is eroded in a process known as notching, leaving an unstable mass of sand above the notch. The mass of sand then develops tension cracks and slumps off. Slumping or avalanching of the dune face can be caused by the infiltration of water into the face of the scarp due to combined high water level and wave impact; the added water increases the sand mass weight and initiates a failure (Palmsten and Holman, 2011). In models, scarp erosion is generally initiated when the beach slope exceeds a user-defined threshold, and is modeled with an arbitrary avalanching parameter (Deltares, 2018). In this regime of scarp erosion, eroded volume of sediment is often underpredicted by models (de Winter et al., 2015; Seymour et al., 2005). Scarps are potentially highly erosive beach features, and while models such as those by Palmsten and Holman (2005), Erikson et al., (2007), or the Xbeach avalanching parameter (Deltares, 2018) can aid in predicting the erosion of a scarp after its formation, these models do not have a good way of predicting the time and location of scarp formation, which is crucial to predicting dune vulnerability and total erosion volume.

1.1 Mechanisms of Process Driven Scarp Formation

Scarps formed by process controls are driven by shallow slope failures in the swash zone when a concentration of wave energy occurs on the beach face, which can occur due to a steep topographical slope or due to water level (tidal level, surge) conditions (Sherman and Nordstrom, 1985). While slope stability prior to scarp formation in the swash zone has not previously been studied, research focusing on momentary liquefaction of sediments under waves, research looking into the effect of beach groundwater elevation on beach stability, and studies focusing on the effect of sediment moisture content on shallow sediment slope stability provide useful context to explore the mechanisms controlling the time and location of dune scarp formation.

1.1.1 Swash dynamics and runup

In the swash zone, the infiltration of water from swash bores can have a significant impact on sediment transport. On the time scale of single swash events, horizontal infiltration is negligible, and vertical infiltration impacts the surficial sediments in two ways. First, seepage forces caused by pressure gradients within the sand can alter the effective weight of the sand; the mechanism for this is discussed in section 1.1.3. Vertical infiltration can also alter the boundary layer velocity profile, moving it closer to the sediment-fluid interface during infiltration and away from the sediment-fluid interface during exfiltration (Turner and Masselink, 1998). Movement of the boundary layer velocity profile can have an impact on bed shear stresses. The impact of both these processes on sediment transport has been captured with the implementation of a modified Shields parameter that changes over the swash cycle (Butt et al., 2001; Turner and Masselink, 1998). Landward of the swash zone, there are several metrics used in parameterizing dune erosion that can be applied to scarp formation. The Sallenger framework is often used to predict the dune erosion regime and predict when dune retreat, overtopping, and inundation will occur (Sallenger, 2000). De Schipper et al., (2017) apply this framework to scarp development, noting that if the maximum wave runup is between the scarp toe elevation and scarp crest elevation, the scarp will migrate landward. If the maximum runup is greater than the scarp crest elevation, it will be destroyed. While Sallenger's framework for erosion regime is often used in conjunction with Stockdon's formulation for the 2% exceedance value of runup (Stockdon et al., 2006), Palmsten and Holman find in a wave tank study that the 16% exceedance value of runup is the best predictor of dune erosion (Palmsten and Holman, 2011).

1.1.2 Groundwater levels and sediment suction

Groundwater dynamics also have an impact on the stability of the beach slope. When the partially saturated beach face is impacted by swash, the beach water content rapidly

increases due to infiltration from swash events, and then slowly declines as the sediments drain. The infiltration takes place as a partially saturated flow, and is an important element to the understanding of scarp formation. As the swash zone progresses landward, either due to storm surge or a rising tide, water from a progressing swash lens infiltrates down through the sand to form a bulge of water beneath the swash zone (Heiss et al., 2015). A diagram of spatial relationship between the groundwater bulge and the swash extent is given in Fig 1, from Heiss (2015).

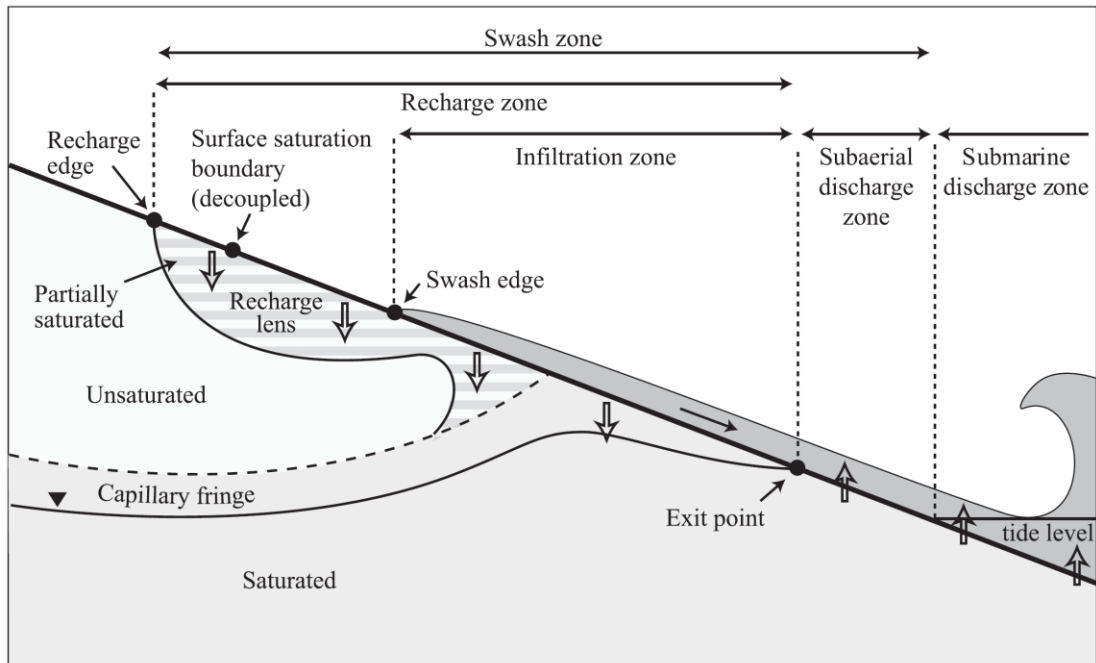


Figure 1: Diagram of the subsurface hydrodynamics in the swash zone, from Heiss (2015)

Laboratory and modeling studies have shown that an elevated groundwater table within a beach can lead to offshore sediment transport (Bakhtyar et al., 2011; Horn et al., 2007). As infiltration and elevation of the groundwater table increase during a storm, the suction force between sand grains due to surface tension between grains, often called matric suction, decreases (Cho and Lee, 2001). Matric suction is due to the capillary force that effectively holds sand particles together in partially saturated sediments (Holtz and Kovacs, 1981). The matric suction force decreases as the moisture content in the sand increases (Krahn and Fredlund, 1971). Near-surface slope stability can change dramatically due to small changes in matric suction, and the reduction in matric suction forces has been identified by Godt et al. (2009) as a trigger for shallow landsliding in slopes composed of permeable soil.

1.1.3 Partial momentary liquefaction

In a soil, excess pore water pressure can develop during rapid drawdown events like tsunami drawdown (Yeh and Mason, 2014) and waves (Mory et al., 2007; Qi and Gao, 2018) when the total stress at the surface is quickly reduced. If the drawdown occurs faster than pore pressures within the soil can dissipate, a negative gradient in excess pore water pressure can develop, where the excess pore water pressure higher in the soil is less than the excess pore water pressure lower in the soil. If this excess pore water pressure exceeds the weight of the saturated soil, the effective stress becomes zero and liquefaction occurs (Holtz and Kovacs, 1981).

Under hydrostatic conditions for saturated sand, the equation for total stress can be written as:

$$\sigma' = \sigma - u = h * \gamma_{sat} - h * \gamma_w, \quad (1)$$

where σ' is the effective stress, σ is the total stress, and u is the pore pressure at depth h (Holtz and Kovacs). γ_{sat} is the saturated unit weight of the sand, and γ_w is the unit weight of water. During a rapid drawdown event, excess pore pressure (p_e) develops within the sand. We can write the excess pore pressure in terms of excess pressure head using the relationship

$$h_e = p_e / \gamma_w. \quad (2)$$

Thus, Equation (1) can be rewritten as

$$\sigma' = h * \gamma_{sat} - (h + h_e) * \gamma_w, \quad (3)$$

By its definition, liquefaction occurs when the σ' equals zero. Therefore, Equation (3) can be written as

$$h * \gamma_{sat} = (h + h_e) * \gamma_w. \quad (4)$$

Equation (4) can be rearranged as

$$h * (\gamma_{sat} - \gamma_w) = h_e * \gamma_w. \quad (5)$$

To make this equation more general, this equation can be applied between two points of known excess pore water pressure head in the sand by rewriting as

$$\delta z * \frac{(\gamma_{sat} - \gamma_w)}{\gamma_w} = \delta h_e, \quad (6)$$

Where δz is the difference in elevation between two pressure sensors in the sand and δh_e is the difference in excess pore pressure head between two sensors. Note that this derivation assumes δh_e refers to subtracting the excess pore pressure head at the upper sensor from the excess pore pressure head at the lower sensor. To use an upward z-axis, we will multiply both sides by -1 and define δh_e as the difference between the upper and lower sensors. Therefore,

$$\frac{\delta h_e}{\delta z} = \frac{h_{e_{upper}} - h_{e_{lower}}}{z_{upper} - z_{lower}} = -\frac{\gamma_{sat} - \gamma_w}{\gamma_w}, \quad (7)$$

For typical void ratios of sands, γ_{sat} is in the range between 18.9 – 20.6 kN/m³, and γ_w is 9.81 kN/m³. Therefore, the final expression for the critical negative excess pore pressure gradient to induce momentary liquefaction for our experiment is

$$\frac{\delta h_e}{\delta z} \sim 0.92 - 1.10. \quad (8)$$

However, complete momentary liquefaction is not necessary to cause a sediment instability. Any negative gradients in $\delta h_e / \delta z$ represent a decrease in effective stress between sand grains from the hydrostatic condition. Tonkin et al. (2003) identified the occurrence of severe scour events around a submerged cylinder subject to regular waves when the excess pore pressure head gradient was half of what was necessary for total momentary liquefaction, showing that even small negative excess pore pressure head gradients can impact erosion.

We present data from a near-prototype dune erosion experiment involving the erosion of a model dune under hurricane conditions. Using data collected from moisture sensors, pressure sensors, and a line-scan lidar, we examine water table dynamics, moisture content, partial momentary liquefaction, and changes in slope over the course of a hurricane to better understand the physical drivers of scarp formation and growth. Recommendations for the more accurate representation of scarp formation within coastal models are discussed.

2. Methods

2.1 *Experimental Setup*

Due to the logistical challenges of collecting data in the field during significant dune erosion events, data on the subsurface hydrodynamics of dune erosion is limited. For this reason, an ambitious lab experiment was designed to make it possible to collect detailed, high frequency data on the processes that contribute to dune erosion. The experiment took place in the NSF NHERI O.H. Hindsdale Wave Laboratory Long Wave Flume (LWF) at Oregon State University. The channel of the LWF is 104m long, 3.7 m wide, and 4.6m tall. The piston-style wavemaker is capable of generating waves up to 1.7 m at a maximum water depth of 2.7m. The wavemaker is equipped with active absorption, but this functionality was turned off at significant wave heights above 0.90m due to mechanical limitations of the wavemaker.

The dune was constructed using sand removed from the South Beach jetty in Newport, Oregon and compacted with a vibrating plate compactor in 1 ft lifts to achieve a compaction near that of a natural dune. The similarity in compaction of the prototype dune and a natural dune was confirmed with Dynamic Cone Penetrometer (DCP) testing in the lab and the field. The sand was poorly graded with a d_{50} of 0.18mm. The initial dune profile was selected for the presence of its berm seaward of the main dune and its ideal dimensions when scaled to the size of the flume, and was based on a 2012 survey of a dune system in Mantoloking, New Jersey.

The experimental wave conditions were scaled from observed conditions during Hurricane Sandy in 2012. The water levels were based on data observed at the Atlantic City NOAA Tides and Currents Station, and the significant wave heights and wave periods throughout the duration of the storm were based on the random phase spectral model WAVEWATCH III offshore of Mantoloking. Wave conditions and dune geometry were scaled using a two free parameter scaling method developed specifically for beach and dune erosion processes (Van Rijn et al., 2011). The two free parameters used were the sediment size scale ($n_{d50} = 1.89$) and the depth scale ($n_h = 2.5$), which we used to calculate the length scale ($n_l = 2.49$) and the time scale ($n_T = 1.58$). The scaled water depth, wave height, and wave period data were fit with exponential curves and discretized into 47 individual wave trials, which were converted to time series using a TMA spectrum. Wave trials contained 300 waves each, and ranged from approximately 20-40 minutes in length depending on wave period. Wave energy was allowed to settle between trials for between 1-2 hours while

instrument adjustments and bathymetry surveys took place. Figure 2 shows the forcing conditions used in the experiment.

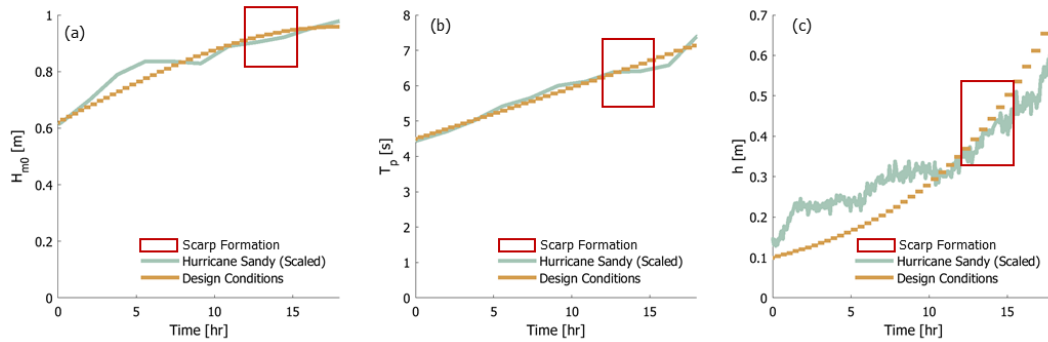


Figure 2: Forcing conditions for experiment: (a) significant wave height, (b) wave period, and (c) water level. Red squares show the time period of scarp formation.

2.2 Instrumentation

The interior of the dune was instrumented with pressure sensors and moisture sensors during its construction. 15 Druck 1800 pressure sensors and 30 Teros-10 moisture sensors were deployed in a way to enable the capture of both the effects of individual waves within the upper parts of the dune and water movement deeper in the dune. Both types of instruments collected data at 100 Hz. Swash velocities were captured with profiling acoustic Doppler velocimeters (ADV), and there were also a set of offshore ADVs and wave gages used for other analyses.

To measure runup and track the erosion of the dune throughout the experiment, a Reigl Z390i line-scan lidar (6mm accuracy, 0.001 deg vertical angle resolution) was set up on an instrument cart above the flume to provide a view of the dune and berm. Throughout the wave trials, the lidar continuously scanned along a single transect at approximately 2 Hz, capturing the water surface elevation, the changing dune profile, and runup elevations. Figure 3 shows a diagram of the sensors referenced further.

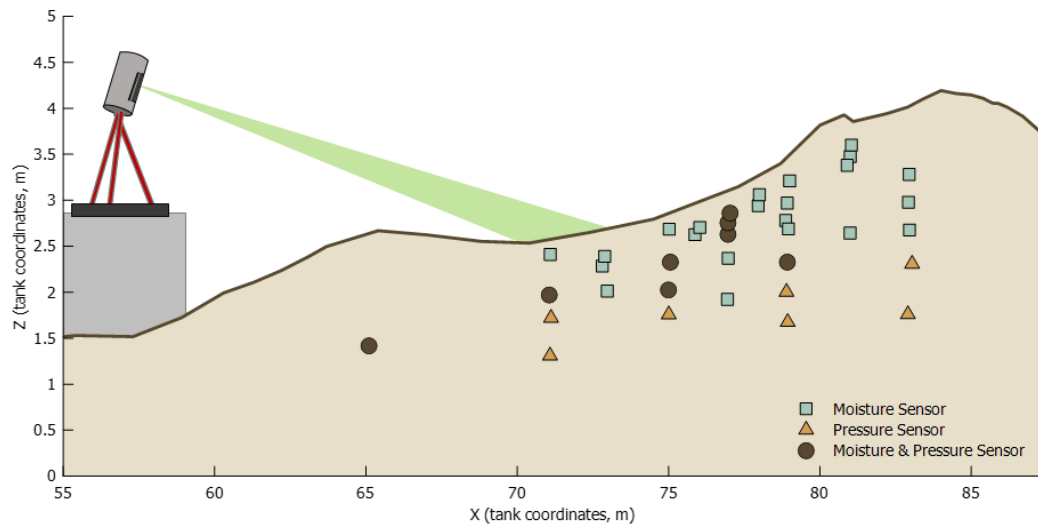


Figure 3: A selection of instrument locations within the dune

The changing bathymetry of the underwater beach profile was measured using a Multiple Transducer Array (MTA) consisting of 32 sonar transducers spanning the width of the flume. The MTA was attached to the underside of an instrument cart and slowly driven along the length of the flume after every wave trial to measure the bed level.

2.3 Signal Processing

2.3.1 Moisture Sensors

To calibrate the Teros-10 moisture sensors used in the experiment, we started by calibrating 15 sensors in groups of 5 in a sand sample at six different water contents. These water contents ranged from air-dried sand (gravimetric water content of approximately 0%) to the highest saturation possible within the calibration setup (gravimetric water content of 20-30%). At each water content, the sensors were buried according to manufacturer recommendations several times to calculate an average voltage reading for each water content. The calibration data for each sensor was fitted with a cubic function; however, while the calibration curves were similar between sensors, differences in shapes in the curves seemed to be a function of the water contents they were tested at. For this reason, we chose to average the calibration curves for the 15 sensors tested, and apply the final averaged curve to all sensors.

2.3.2 Pressure sensors

The Druck 1800 pressure sensors used in the experiment were calibrated initially using calibration coefficients provided by the manufacturer. The data was then processed in

two ways to identify the magnitude of pressure fluctuations for use in understanding liquefaction events, and to track the water level throughout the course of the experiment.

For an analysis of liquefaction, we isolated the excess pore pressure to identify the time periods in which frequent negative excess pore pressure gradients occurred (Equation 7). For the sensors of interest located in the swash zone, we filtered the pressure sensors with a 30 second moving minimum filter, which was then smoothed. This allowed us to analyze the influence of single waves on gradients in excess pore pressure within the dune while removing the effects of a locally rising water table.

To track the interior dune water level over time, we first had to offset the output of the calibrated pressure sensor signal to match their expected output. Due to dune construction logistics, the pressure sensors were deployed within the dune approximately six months before the experiment, and were unable to be balanced to ensure their output was zero with zero load. This was obvious in some sensors, which consistently showed a considerable offset from the water table elevation calculated from other sensors at the same cross-shore location. To balance the signals during processing, we determined the offset between the sensors' reading at the start of the first trial of the week, after the water table was still in the dune for several days, and the expected reading based on the water level at the exterior of the dune. The water table within the dune is assumed to be flat after having the weekend to equilibrate to match the water level at the exterior of the dune, especially considering that sand is a well drained sediment. After these offsets were determined and applied, the pressure signals were smoothed with a 4 minute moving average to remove fluctuations in the water table due to short time-scale infiltration events. When there were multiple sensors stacked vertically at the same cross-shore location, the lowest sensor in each stack was used for the calculation of the water level.

2.2.3 Lidar

The lidar scans were rectified using a plane rectification method developed from O'Dea et al. (2019). The plane rectification method uses 10 planes oriented in different directions around the scanner to match the frame scan taken prior to each trial to a baseline scan minimizing the least square errors and generating the corresponding transformation matrix.

The baseline scan is developed from two scans taken prior to the first trial of the vegetated dune without moving the lidar between them. The first scan is low resolution, but captures a large view of the wave lab, including wave lab reflectors. The second scan is higher resolution, but only captures the flume. We used a combination of permanent wave lab

reflectors and temporary reflectors installed for the experiment in the low resolution scan to calculate a transformation matrix for the baseline scan. This transformation matrix was then applied to the high resolution scan to rotate it so it could be used as the baseline scan for plane matching.

After the baseline scan was finalized, each scan was initially rotated with a rough fixed transformation matrix generated manually in CloudCompare. This transformed the scan from the lidar's coordinate system to the wave lab coordinate system to allow the reflector-finding code to search in the correct location for reflectors. The reflector-finding code rotates the scan and generates a transformation matrix by identifying three reflectors and minimizing the least square error between the reflectors and their surveyed locations. This transformation is intended to rectify the scan as closely to the baseline as possible, but due to the limited number of reflectors and the fact that the reflectors visible in the scans changed throughout the experiment, this rectification was not sufficient as a final transformation. However, it was necessary to enable the plane-matching algorithm to function correctly.

The plane transformation matches points on 10 planes at different locations along the flume wall in the baseline and the scan previously rotated using the reflectors. The plane-matching code trims the baseline scan and frame scan into only the points present on the selected planes. Then, 100 points are sampled at random from those points, and a least squares fit is used to match them to the mathematical plane generated using the same procedure in the baseline scan. After the frame scans were rectified, the final transformation matrix generated for each trial was used to rectify the data from each line scan. Line scans are effectively a series of scans along a single transect at approximately 2 Hz for the duration of each trial. When filtering this data, the sand surface was identified by using a 25-second moving minimum filter in time to remove points captured during swash events. The swash depth was calculated by subtracting the sand surface from the original data, and the runup extent was defined as the furthest point landward where the swash depth was less than 2 cm.

3. Results

Our results focus on observations of sediment mechanics during the formation of the dune scarp, with emphasis on the period of time between trials 36 and 41. The results are split into 4 sub-sections; we will first present the changing dune scarp morphology, then we will show how the total hydraulic head, the sediment moisture, and the sediment pore water pressure gradients due to setup and swash combinations influence the interior dune sediment hydraulics and their contribution to scarp formation.

3.1 Dune scarp morphological development

The constructed initial experimental beach profile consisted of a berm situated seaward of a beach dune. The berm eroded over the first 10 of 47 total trials. After the berm eroded, the remaining beach profile shape was concave in curvature, where a mildly sloping beach met a steeper dune face. The concave beach profile continued to recede landward in time between trials 36-41. Figure 4 shows a cross shore cross section of the progression of the dune shape throughout the experiment.

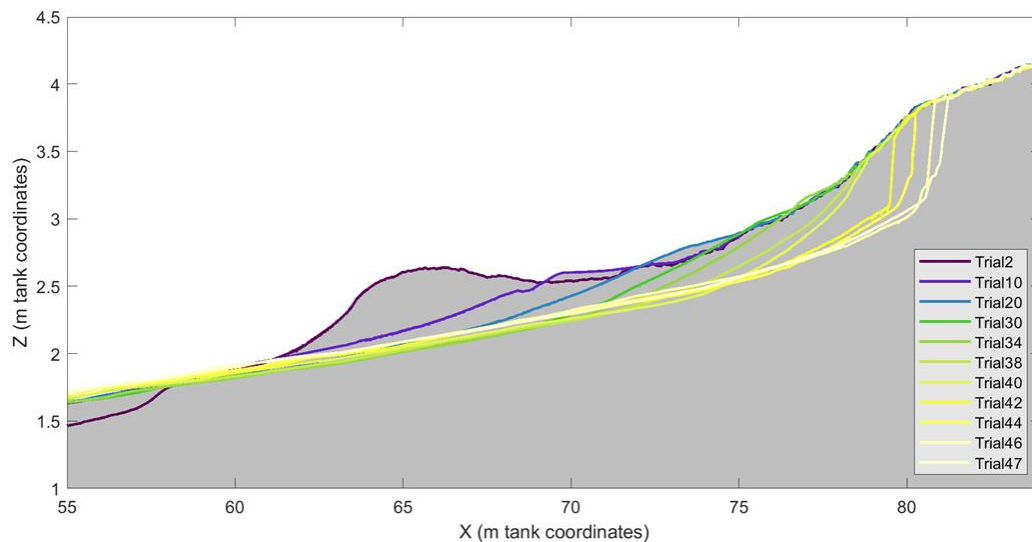


Figure 4: Changes in the dune profile over the course of the experiment. Note that the intervals between presented profiles are uneven, as the dune eroded slowly at first and quickly at the end of the experiment.

After the berm eroded, the slope of the upper beach profile steepened, until the beach slope failed and turned into a vertical scarp during trials 36-41. After the development of the scarp, the erosion mechanism shifted to the well-studied phenomena of slumping (e.g. Palmsten and Holman 2011), in which the face of the scarp gets wet from swash collision events and the increase in sediment weight leads to collapse. After the shift in erosion

mechanism, the scarp quickly receded landward (trials 42-47). Figure 5 shows the development of the scarp through the later trials of the experiment.

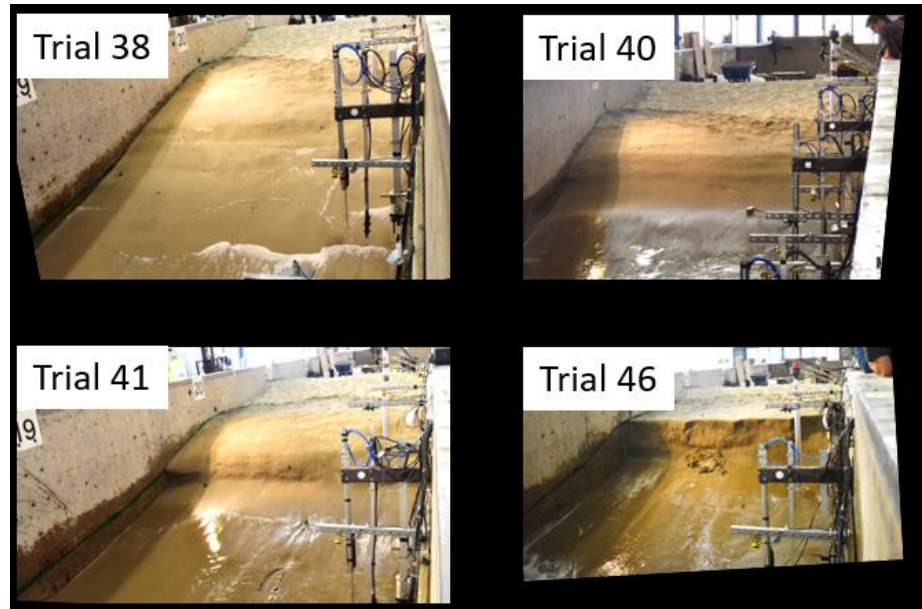


Figure 5: Photos of the dune as it eroded

Figure 6 shows a zoomed in progression of the dune profile in the immediate location of the scarp formation as well as the location of relevant instrumentation within the dune. The intervals displayed are uneven because as the slope steepened in the later trials, it receded much more rapidly. The dashed line is a visual representation of the total hydraulic head of the water within the dune, and is calculated by converting the averaged pressure signal to an equivalent water depth above the sensor.

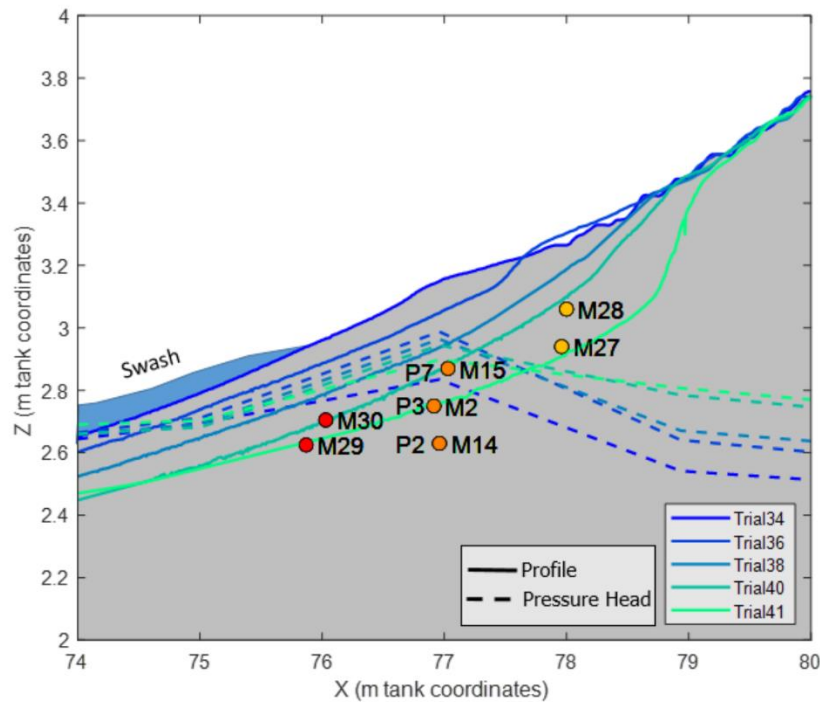


Figure 6: Changes in the dune profile and total hydraulic head during the period of scarp formation. Sensors referenced later are also included.

Figure 7a uses the elevation of the sand surface, which was collected continuously by the line-scan lidar, to show the development of the scarp in space and time. The x axis represents time, the y axis represents the cross shore location, and the color shows the change in dune elevation at each location relative to the beginning of trial 36 (see Figure 6 for reference profile). Blue represents erosion from the sand surface at the start of trial 36, while red represents accretion. There is an erosion hotspot that develops at a cross shore location of about 77 meters and grows until it becomes a scarp. There is no accretion anywhere on the profile during this time period. Figure 7b shows a time stack of the slope as the scarp develops. There is an obvious break in slope that begins at approximately meter 77 at the beginning of trial 36, and moves landward and steepens as the waves get bigger and water level increases. The break in slope leads to the creation of the dune scarp. For reference, we consider the incipient scarp to be formed by the end of trial 40. Figures 6-7a,b show the development of the scarp morphology in time; we will refer to these figures again in the next sections as we examine the hydraulic and hydrodynamic mechanisms contributing to the dune scarp formation and development.

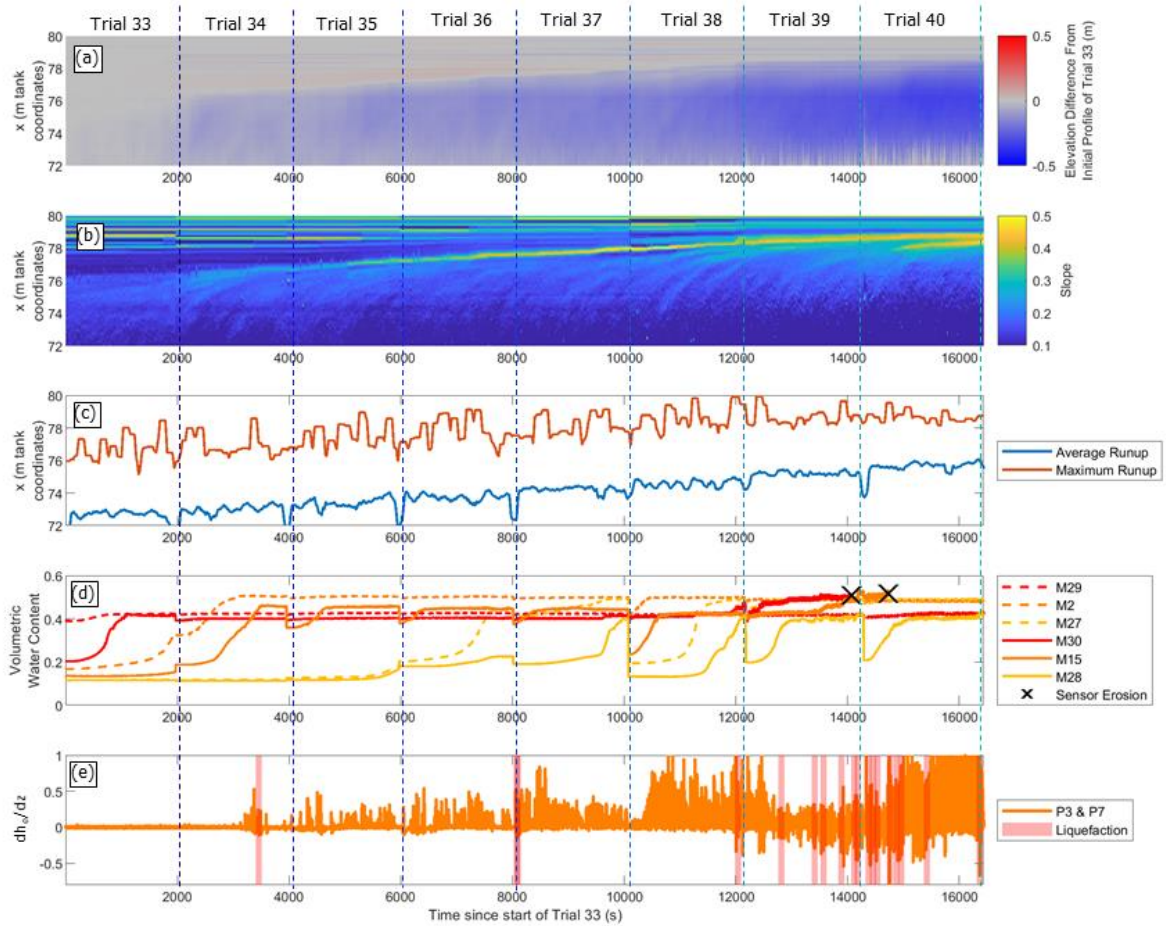


Figure 7: Changes in dune properties from trial 33 – 40: (a) time stack of erosion across profile in reference to the initial profile of trial 36, (b) time stack of slope, (c) average and maximum runup (d) changes in moisture content of sensors in the upper 30 cm of sand at meters 76, 77, and 78, and (e) excess pore pressure gradients between sensors P2 & P3 and between sensors P3 & P7, with negative gradients shaded in red.

3.2 Dune interior pressure head

Figure 6 shows the dune surface profile change in relation to the exterior water level and the pressure head within the dune during the time period of scarp formation (trials 36-41). The exterior water level refers to the water level interfacing between the dune and the average free surface water elevation outside of the dune (Figure 6, $X \leq 74.5$ m tank coordinates). The pressure head refers to the pore water pressure within the dune. In figure 6, this is converted into an equivalent water depth above the sensor. The interior dune pressure head is based on a moving average of the data collected from pressure sensors low in the dune (Figure 3), and is calculated at the end of each trial to show the full effect of waves on the dune interior pressure head. Under hydrostatic conditions, this value would represent the water level inside of the dune. The interior pressure head is relatively constant between trials

36-39; however, during these trials it is significantly elevated above the pressure head at the exterior of the dune. The elevation of the total hydraulic head in the interior of the dune is caused by an increase in the interior water table elevation due to infiltration from runup in conjunction with a buildup of dynamic pressure when excess pore pressure caused by a swash event within the dune cannot dissipate before the arrival of the next wave. A bulge in the water table underneath the swash zone is suggested by the elevated total hydraulic head at that location, and confirmed with moisture sensor data. While the pressure head appears to stay the same between trials 36 and 39, the elevation of the sand surface changes. During trials 38, 40, and 41, the pore water pressure head (converted to a hydrostatic water depth and plotted with a dashed line) is greater than the elevation of the sand surface (solid line, Figure 6) above the sensor, demonstrating that, on average, the pore pressure in the sand is greater than it would be under fully saturated conditions. We infer that the continuous swash events continuously increased the dynamic pressure within the sand before it could fully dissipate, leading to a buildup of water within the dune. The locations of the seven moisture sensors and three pressure sensors most relevant in studying the formation of the scarp are also presented in Figure 6, and will be referred to henceforth.

3.3 Dune sediment moisture content

As the beach slope discontinuity moves landward (Figure 7b), not only is the total hydraulic within the dune changing, but the volumetric moisture content in the surficial sediments underneath the discontinuity are also changing. Figure 7d shows the moisture contents at three locations marked on Figure 6, sensors are located approximately 20 and 30 cm below the initial sand surface. The color of the lines indicates the sensor cross shore position in the dune as colored in Figure 6. If we follow one moisture sensor in time (M15 – orange solid line), we can see that the sediment moisture is decreased at the onset of every new trial; this is due to the experimental progression, where we needed to pause the wavemaker to make measurements and allow the tank to settle after every 300 waves. We can also see that the sensor measurement of volumetric water content increases slowly and then plateaus; it is likely the sand around the sensor has reached saturation at the plateau. At meter 76 (red lines) during trials 33 to 34, the sand reaches saturation at a moisture content of 0.4. However, at meters 77 and 78 (orange and yellow lines), the moisture content at saturation is closer to 0.5 during the same trials. The increased saturation level at meters 77 and 78 could indicate a higher void ratio of the sand in that area. During trials 33 to 37 the moisture sensors at meters 76 and 77 are on the seaward side of the predominant region of swash events

(Figure 6 shaded region), where the sensors at meter 78 are in the active swash region, such that the continuous swash events could be destabilizing local sediments enough to effectively increase their void ratio. The erosion of moisture sensors (marked with an x on Figure 7d) shows an increase of previously saturated sensors over their saturated moisture content just before the sensors erode from the dune.

3.4 Dune sediment partial momentary liquefaction

Instabilities due to partial momentary liquefaction occur when the vertical gradient in excess pore pressure head is less than zero (equation 8). The bigger the magnitude of this gradient, the more significant effect the event is likely to have on beach erosion; a gradient of approximately -1 or less represents full liquefaction. A vertical gradient in excess pore pressure is caused in this experiment when a wave runs up the beach, increasing the pressure throughout the top layer of sand. When the wave draws down, there is an instant decrease in pressure at the sand surface. However, the pressure lower in the sand has not yet dissipated, and thus exerts a force upward on the sand. Figure 7e shows the increase in frequency of partial momentary liquefaction events between sensors between sensors P3 and P7 over the course of trials 36-40. Partial momentary liquefaction events are shaded in light red if their gradient is less than -0.1 to best show the changing frequency of events.

To better understand what drives the partial momentary liquefaction events, we can examine them more closely as the scarp progresses. Figure 8 is an example of several swash events during trial 36, as the slope of the beach first begins to steepen. Figure 8a shows a time stack of the swash depth and the runup extent throughout a 200 second time period. The cross shore location of the sensors buried at meter 77 is marked with a dashed line. Figure 8b displays the swash depth at the cross-shore sensor location, showing that the biggest swash event impacting the sensors during this time period was approximately 20 cm deep measured from the surface of the sand. Figure 8c shows the volumetric water content of the three sensors at meter 77. The moisture sensors are offset from each other in the figure, and colored by their water content. M2 has a higher water content than both M14 and M15, suggesting the void ratio of the sand may be larger at that depth. Fluctuations in the moisture content during these events are minimal. Figure 8d shows the fluctuations in excess pore pressure gradient caused by the swash events displayed in the first two panels. While there are fluctuations in the pressure gradient, they are small and gradual, neither set of sensors records a significant partial momentary liquefaction event. The gradient also has ample time to dissipate before the next swash event occurs.

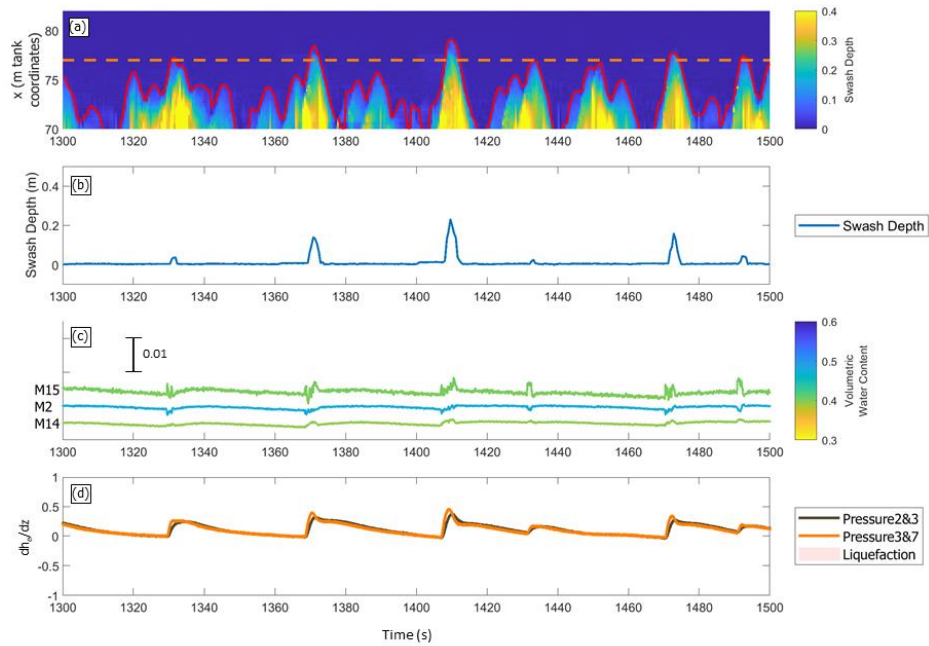


Figure 8: A selection of 200 seconds of data from trial 36: (a) time stack of swash depth, with runup extent marked in red and the cross-shore location of sensors marked in orange, (b) time series of swash depth at location of sensors, (c) volumetric moisture content for sensors M14, M2, and M15, colored by their absolute moisture content, (d) excess pore pressure gradients between sensors P2 & P3 and between sensors P3 & P7, with negative gradients shaded in red.

Figure 9 shows several swash events during Trial 38, which has a similar interior water level, but less sand covering the sensors. In addition, as the wave height and water level greater than that of trial 36, there are more swash events impacting the cross-shore location of the sensors; the setup of the figure is the same as Figure 8. The largest swash depth in this time period is 40 cm (Figure 9b), about twice that of the swash depth in the previous time period shown in Figure 8. Additionally, there is a significant difference in the magnitude and shape of negative excess pore pressure gradients caused by the swash events (Figure 9d) between the two time periods. Between sensors P3 and P7, a negative pore pressure gradient develops as the wave draws down the beach face. Finally, we can see that during the time period, the volumetric water content at the top sensor (M15) decreases during each swash event, while the middle and lower sensors (M2 and M14) show slight increases in moisture (Figure 9c), indicating that the top layer of sand could be compressed during the swash event, squeezing water into lower parts of the dune. After the swash event, water infiltrates down into the sand causing a subsequent spike in moisture content, which slowly dissipates as the

water infiltrates away from the sensor. The pattern shifts toward the end of this time series, where M15 starts responding to wave effects by increasing, and M2 decreases.

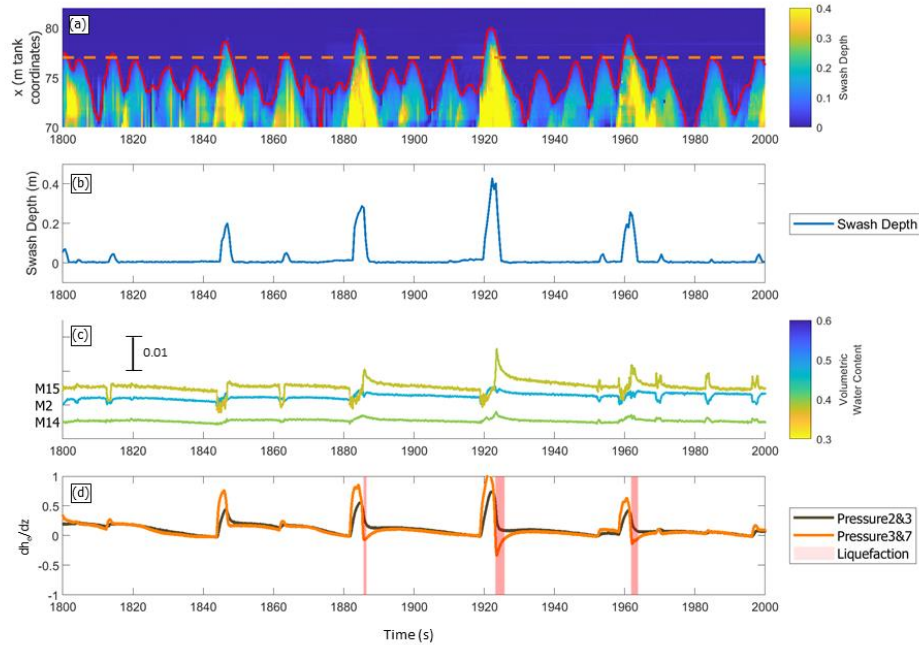


Figure 9: A selection of 200 seconds of data from trial 38: (a) time stack of swash depth, with runup extent marked in red and the cross-shore location of sensors marked in orange, (b) time series of swash depth at location of sensors, (c) volumetric moisture content for sensors M14, M2, and M15, colored by their absolute moisture content, (d) excess pore pressure gradients between sensors P2 & P3 and between sensors P3 & P7, with negative gradients shaded in red.

Figure 10 shows 200 seconds of swash events during Trial 40. By trial 40, the scarp is already formed and the scarp location has receded landward to meter 79. The swash events impact the cross-shore location of interest with greater frequency, although the maximum swash depth is only about 20 cm at meter 77. The decrease in swash depth is potentially due to the steepening beach slope causing a change in momentum of the swash bores. The fluctuations in excess pore pressure are much greater than the previous two trials, which is likely due to the decreased sand cover above the sensors and the more seaward location of the sensors relative to the scarp position when compared to the previous trials. While M15 has previously eroded out of the dune, the volumetric water content at the deeper sensors M2 and

M14 decreases during the runup phase and increases during the drawdown phase with dilation of the bed.

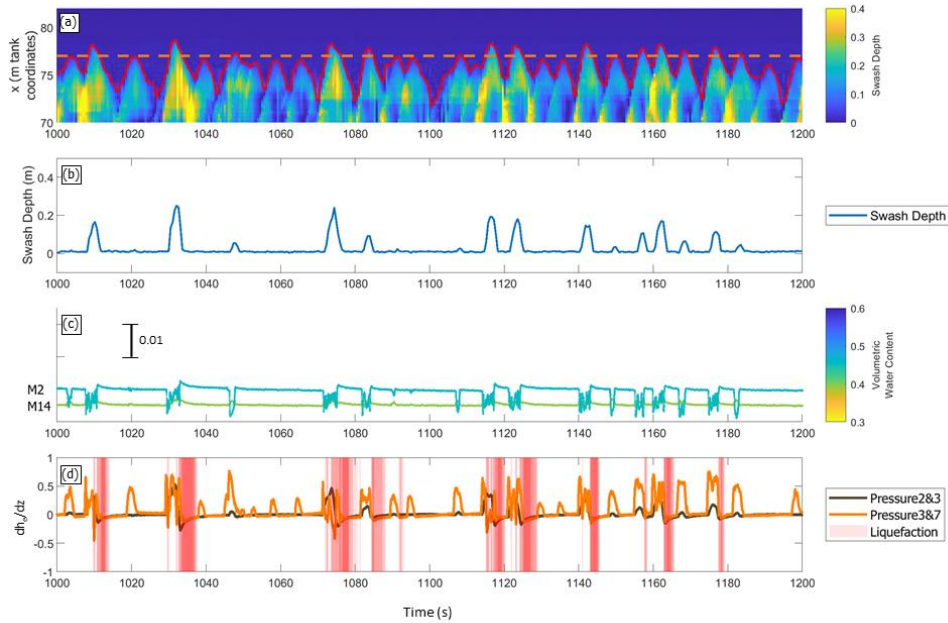


Figure 10: A selection of 200 seconds of data from trial 40: (a) time stack of swash depth, with runup extent marked in red and the cross-shore location of sensors marked in orange, (b) time series of swash depth, (c) volumetric moisture content for sensors M14, M2, and M15, colored by their absolute moisture content, (d) excess pore pressure gradients between sensors P2 & P3 and between sensors P3 & P7, with negative gradients shaded in red.

4. Discussion

Results show that there are three hydraulic mechanisms aiding in the formation of the dune scarp: 1) the increase in volumetric water content of the dune sediments, which lead to a reduction in matric suction 2) the elevation and pressurization of the water table within the dune, and 3) the vulnerability of the surficial sediments to partial momentary liquefaction during swash bore drawdown. To understand the way the subsurface hydrodynamic processes impact slope stability, we can use the analogy of a block sliding on an inclined surface. In the classic physics problem, the gravity force of the block is driving the block down the slope, while the friction force is resisting its slide. If we think of a shallow layer of a beach slope as the sliding block, a reduction in matric suction and an increase in the frequency and magnitude of partial momentary liquefaction events will both reduce the ‘friction’ force, while an increase in beach slope will increase the ‘driving’ force.

Moisture content increases as the water level at the exterior of the dune increases and water seeps toward the interior of the dune. In addition, due to infiltration from swash, a local increase in the total hydraulic head also develops, and moves landward as the runup extent increases, increasing the water content near the sand surface. High water contents create a reduction in matric suction, reducing the resisting forces on a slope. There are two sensors that erode during the time period presented in Fig 7, and both are preceded by moisture contents elevated above their apparent saturation values, suggesting that the increase in moisture content and subsequent reduction in matric suction force is necessary for erosion. For the water content near the surface to be elevated to values that reduce the matric suction enough to lead to erosion, the water table must be at or near the sand surface, otherwise the water will just infiltrate downward into the dune.

As the exterior dune water level increases throughout the experiment and the waves increase in height and period, the bulge in the apparent water table (total hydraulic head) beneath the swash zone rises and approaches the elevation of the surface of the dune. After the apparent water table reaches the sand surface and the dune is saturated, the pressure of the pore fluid continues to increase beyond the hydrostatic condition as pressure induced by increasingly frequent swash events can no longer dissipate between waves. We quantify this process by calculating the difference between the sand surface elevation and the total hydraulic head based on the moving average of the pressure signal from sensors at meter 77. If the sand surface elevation (SSE) is above the total hydraulic head (THH), then $SSE - THH > 0$ and the upper layer of dune is unsaturated or partially saturated. If $SSE - THH <$

0, then the pore fluid is pressurized above what would occur in a saturated dune in its hydrostatic condition ($SSE - THH = 0$).

Figure 11a-f shows the relationship between $SSE - THH$, the swash elevation, and the frequency and magnitude of liquefaction events between sensors P3 and P7 during trials 35-40. The x-axis of subplots a-f represents $SSE - THH$, the y-axis represents the swash depth (the depth of the swash layer measured from the surface of the sediments to the swash bore free surface), and the color of the points corresponds to the magnitude of the momentary pore pressure head gradients ($\delta h_e / \delta z$). Cool colors represent negative gradients (partial momentary liquefaction events), while warm colors represent positive gradients (sediment stabilizing events). For clarity, data points in which the negative excess pore pressure gradient was less than -0.1 are larger than the rest of the data points. Figure 11g shows the profiles and calculated total hydraulic head at the end of each of the trials shown in a-f for reference.

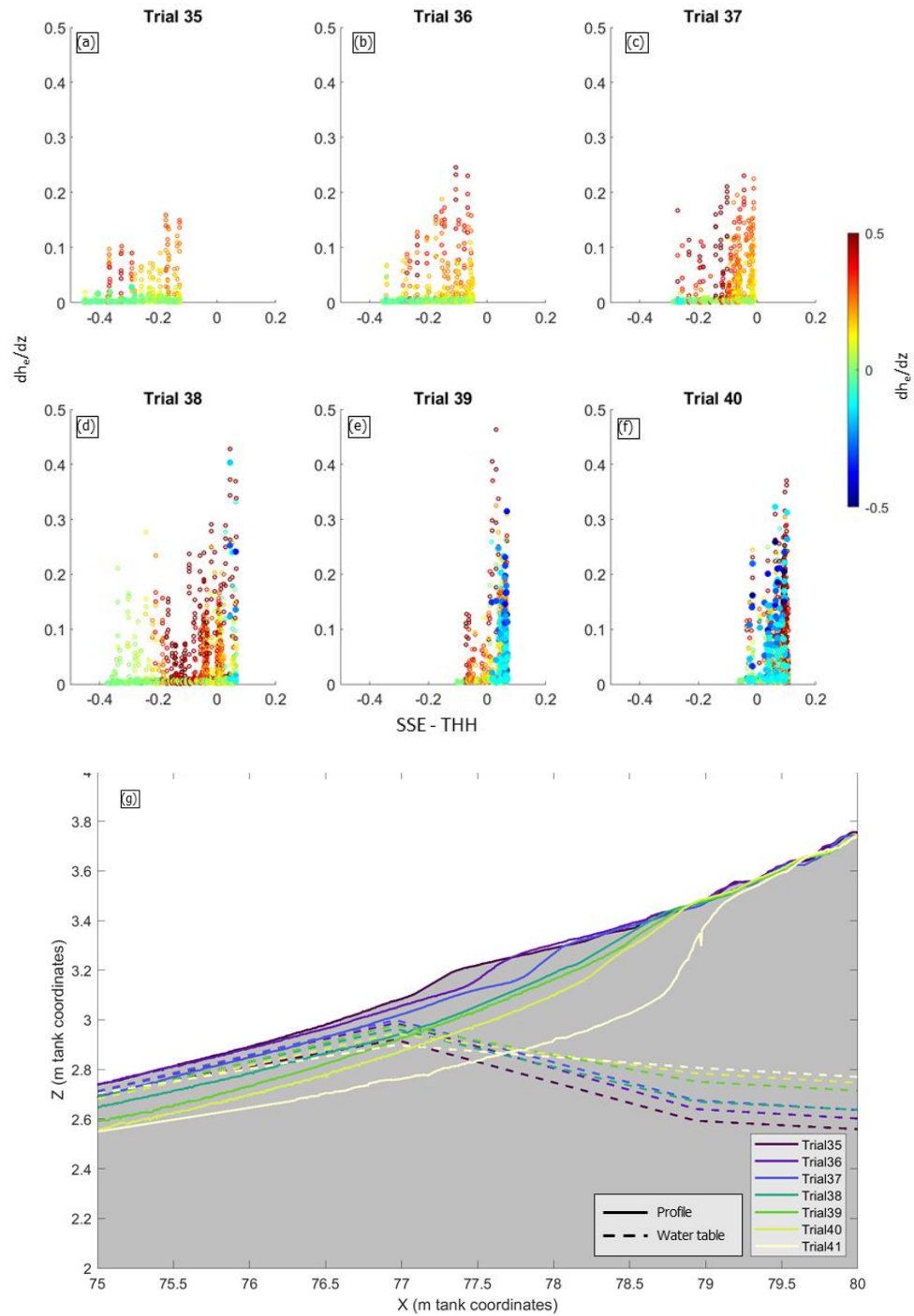


Figure 11: (a) – (f): Correlation between SSE - THH, x-axis, swash depth (y-axis), and magnitude of partial momentary liquefaction events (color). (g) shows the progression of the scarp and the total hydraulic head throughout the trials displayed in (a) – (f)

Figure 11 highlights a few different mechanics. First, we notice that there is a positive correlation between the greatest swash depths and the largest $SSE - PPH$. We also notice that the partial momentary liquefaction events mostly do not start occurring until the largest $SSE - PPH$ in Trial 38. There are more stabilizing ($\delta h_e / \delta z > 0$) events than destabilizing ($\delta h_e / \delta z < -0.1$) events, and that the stabilizing events occur at all recorded values of $SSE - PPH$ and swash depth across the range of swash depths. Finally, we notice that some of the stabilizing events have greater swash depths than some of the destabilizing events. The next paragraphs highlight some of the details and consequences of our observations.

When the destabilizing partial momentary liquefaction events occur, they show a correlation to the swash depth at the time they occur. The higher-magnitude partial momentary liquefaction events (denoted with the darker blue colors) increase with increasing swash depth. While not all swash events at high depths show a destabilizing force, the partial momentary liquefaction events occurring at a high swash depth tend to be more forceful than those occurring at smaller swash depths. This is illustrated by a color gradient in partial momentary liquefaction events from low swash depth to high swash depth, where the intensity of the point color corresponds to the intensity of the partial momentary liquefaction events (Fig 11). We hypothesize that these forceful liquefaction events occur just out of phase with the highest swash events, which means they occur after the water has already begun running down the beach face. This is evident in Figure 9 and 10, when liquefaction events occur after the peak of the swash event at meter 77.

Figure 11a-f also shows the impact of the pressurization of the pore fluid (elevated water table). The majority of partial momentary liquefaction events occur when the dune is saturated and the pore fluid is pressurized above hydrostatic conditions ($SSE - THH > 0$). We hypothesize that this occurs because the pressurization of pore fluids means that the excess pore pressure created by the swash bore is unable to dissipate through a transfer of the load to the soil prior to wave drawdown. If fluctuations in pressure cannot dissipate, the occurrence of large negative excess pore pressure gradients ($\delta h_e / \delta z < -0.1$) as the wave unloads the sand is more likely.

While Figure 11 allows us to analyze the effect of swash depth and total hydraulic head on the frequency of liquefaction events, these metrics do not take the cross-shore migration into account. As we only deployed pressure sensors near the surface at a single cross-shore location, directly observing spatial variations in excess pore pressure head gradients is not possible with these data. However, we can observe patterns in moisture

sensors that vary spatially. Figure 12 shows the wave runup (Figure 12a), moisture sensor data from meter 76 (Figure 12b), moisture sensor data from meter 77 (Figure 12c), and the prevalence of partial momentary liquefaction events (Figure 12d). When waves impact the sensor location, the moisture sensors at meter 76 (M29 and M30) show a decrease in moisture content due to compression of the sand, and a subsequent increase in moisture content as the sand rebounds from the swash bore compression. The sensors at meter 77 (M14, M2, M15) show a similar initial decrease in water content as the swash bore passes. However, the only increase in moisture content at meter 77 occurring subsequent to a decrease of moisture content due to sediment compression is seen in sensor M15 at time $t = 1385$ s; during this event we can see a concomitant partial liquefaction event in the surficial sediments as measured by the pore water pressures at meter 77. In general, we observe the decrease and subsequent increase in moisture content occurring in the context of measured partial liquefaction events at meter 77 where both types of measurements are available. The increase in moisture subsequent to the compression of the sediments under the swash bore could be a sign of partial momentary liquefaction events, which allow us to infer partial momentary liquefaction occurrences both shoreward and seaward of meter 77. During these 200 seconds in Figure 12, the excess pore pressure head gradient at meter 77 only indicates a single partial momentary liquefaction event and the moisture sensor signature at meter 77 shows the same. However, the increases in moisture recorded by both sensors M29 and M30 under the majority of swash events suggest partial liquefaction is more prevalent at that location. The difference in output from the two sensor locations indicates that while the frequency of partial momentary liquefaction events are increasing as the total hydraulic head within the dune and the swash depth increase, the locations of these events are also changing as the scarp migrates landward.

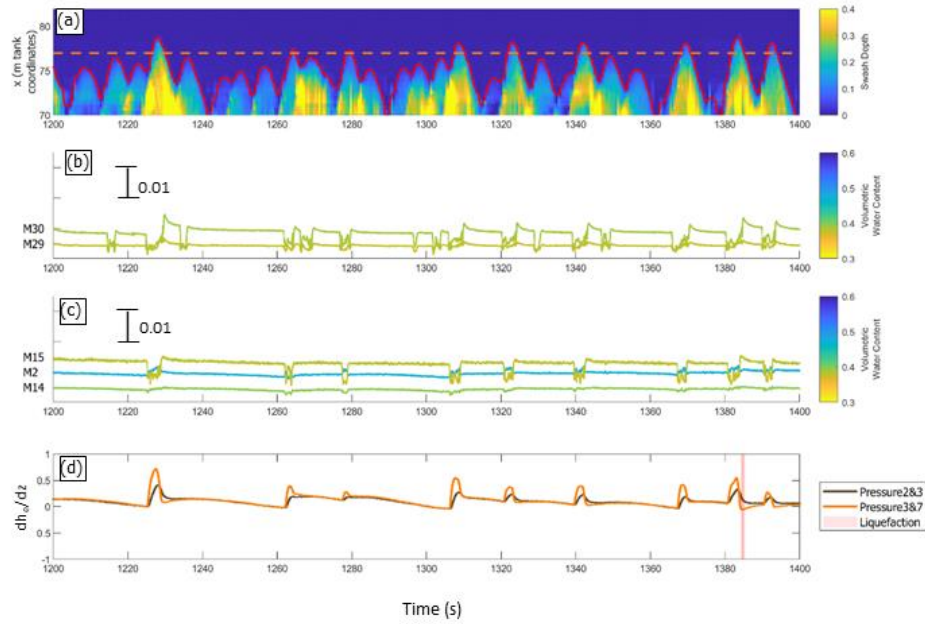


Figure 12: A selection of 200 seconds of data from trial 38: (a) time stack of swash depth, with runup extent marked in red and the cross-shore location of sensors marked in orange, (b) volumetric moisture content for sensors M29 and M30, colored by their absolute moisture content, (c) volumetric moisture content for sensors M14, M2, and M15, colored by their absolute moisture content, (d) excess pore pressure gradients between sensors P2 & P3 and between sensors P3 & P7, with negative gradients shaded in red.

Partial momentary liquefaction events (determined both directly through excess pressure head gradients and through moisture sensor liquefaction signatures) and elevated total hydraulic heads are observed seaward of the slope discontinuity. During Trial 34, partial momentary liquefaction events can be inferred through the moisture sensor data at meter 76 as the slope discontinuity is developing above meter 77. By Trial 39, liquefaction events occurred at meter 77 while the slope discontinuity had progressed to meter 78.5. This indicates that while these destabilizing events are not occurring on the relatively dry face of the developing scarp, the sediments seaward of the scarp are vulnerable to increased erosion and destabilization as runup elevations increase throughout the experiment.

5. Conclusion

The subsurface hydrodynamics involved in the formation of scarps on coastal dunes were studied in a near-prototype lab experiment forced with hurricane conditions in the NSF NHERI O.H. Hinsdale Wave Research Laboratory Large Wave Flume. Water level, wave height, and wave period data collected during Hurricane Sandy were scaled and discretized into 47 trials of approximately 300 waves each, which were used as forcing conditions on a scaled berm-dune profile from Mantoloking, New Jersey. In the first 10 trials of the model storm, the berm eroded, followed by the landward erosion of the beach, creating a concave beach profile. As swash bores continued to collide with the beach a slope discontinuity developed during trial 34, and grew more prominent until it became a vertical scarp by the end of trial 41.

Within the dune, the moisture content and pore water pressure near the dune surface near the location of scarp formation were monitored, and pressure sensors buried deeper in the dune tracked the total hydraulic head at different locations throughout time. The local increase in total hydraulic head and moisture content suggest that an elevated total hydraulic head occurred beneath the swash zone due to infiltration and pressurization from swash events. Beneath the swash zone, patterns in volumetric water contents showed that sensors were saturated at elevations above the still water level, indicating a local increase in water table elevation due to infiltration. At the same time, the pore fluid within the dune increased in pressure due to the increasing frequency of swash events. As the time between swash events decreased, pore pressures could not dissipate before the next swash event arrived. The combination of an increase in the elevation of water table and a buildup of dynamic pressure within the dune led to an elevation in total hydraulic head underneath the swash zone. The cross shore location of the elevated total hydraulic head moved landward as wave height, wave period, and water level increased.

During the period of scarp formation, moisture sensors indicated that the dune became saturated at the sensor location as the scarp progressed landward. Volumetric water contents at saturation ranged from 0.4 – 0.5, likely depending on the void ratio of the sand at the sensor location. After the scarp migrated past the locations of several moisture sensors, they eroded. Their erosion was preceded by a gradual increase in volumetric water content above the apparent saturation of the surficial sediments, potentially indicating bed dilation. Evidence shows that the saturated state of the dune weakens it and contributes to a greater

likelihood of slope failure, as the matric suction force between sand grains in a saturated state is weaker than the matric suction force in an unsaturated state.

Pressure sensors buried near the surface of the dune captured instances of partial momentary liquefaction, which occur during the development of a negative excess pore pressure gradient. The destabilizing partial momentary liquefaction events typically occur just after the peak of an increase in swash depth and as the wave begins to wash back down the beach. When a swash event occurs, it increases the pressure of the pore fluid below it. However, when the surface is quickly unloaded during wave drawdown, the excess pore pressure within the dune has not yet dissipated, thus causing a negative gradient in pore pressure that reduces the effective weight of the sand and destabilizes the dune sediments. The magnitude of these events are correlated with the depth of the swash bores that cause them. In addition, the majority of the partial momentary liquefaction events occur when the dune is saturated and the total hydraulic head is greater than expected for saturated hydrostatic conditions. We also observed a partial momentary liquefaction signature in the moisture sensor data. When partial momentary liquefaction events occur, the moisture sensor data shows a drop, then a sudden increase, indicating that the sand has compressed, then dilated as the swash bore loads and unloads the sediment surface.

As the swash bore runup elevations progress shoreward during the simulated storm event, the sediments at the confluence of the elevated total hydraulic head within the subsurface sediment pore spaces and the location of partial momentary liquefaction events become increasingly vulnerable to erosion. The sediments at and landward of the slope discontinuity are relatively dry and stable in comparison to the adjacent seaward sediments of the slope discontinuity. As such, with increased runup elevations, the vulnerable sediments seaward of the slope discontinuity erode, and the discontinuity continues to progress landward, eventually forming a scarp.

An understanding of the subsurface hydrodynamics of a dune is crucial to predicting potential scarp formation. However, the relationship between subsurface and subaerial dynamics can provide even more insight into the dune morphology. Based on the results of our study, we hypothesize that bore-bore capture events causing high swash depths, large drawdown effects, and the relationship between dune geometry and the changing runup extent could all influence the formation of the initial slope discontinuity and the frequency of destabilizing events. Additionally, the relationship between the location of the increased total hydraulic head and swash runup magnitude could also influence the destabilizing events. Once quantified, such statistics could provide useful input to models such as XBeach to better

define a set of physical criteria leading to the formation of a scarp, and in turn, allow for more accurate predictions of erosion volume during storm events.

6. References

- Bakhtyar, R., Brovelli, A., Barry, D.A., Li, L., 2011. Wave-induced water table fluctuations, sediment transport and beach profile change: Modeling and comparison with large-scale laboratory experiments. *Coast. Eng.* 58, 103–118.
<https://doi.org/10.1016/j.coastaleng.2010.08.004>
- Butt, T., Russell, P., Turner, I., 2001. The influence of swash infiltration - efiltration on beach face sediment transport: onshore or offshore? *Coast. Eng.* 42, 35–52.
<https://doi.org/10.2208/prohe.47.1327>
- Cho, S.E., Lee, S.R., 2001. Instability of unsaturated soil slopes due to infiltration. *Comput. Geotech.* 28, 185–208. [https://doi.org/10.1016/S0266-352X\(00\)00027-6](https://doi.org/10.1016/S0266-352X(00)00027-6)
- de Schipper, M.A., Darnall, J., de Vries, S., Reniers, A.J.H.M., 2017. Beach scarp evolution and prediction.
- de Winter, R.C., Gongriep, F., Ruessink, B.G., 2015. Observations and modeling of alongshore variability in dune erosion at Egmond aan Zee, the Netherlands. *Coast. Eng.* 99, 167–175. <https://doi.org/10.1016/j.coastaleng.2015.02.005>
- Deltares, 2018. XBeach Documentation: Release XBeach v1.23.5527 XBeachX FINAL, v1.23.5527. ed.
- Erikson, L.H., Larson, M., Hanson, H., 2007. Laboratory investigation of beach scarp and dune recession due to notching and subsequent failure. *Mar. Geol.* 245, 1–19.
<https://doi.org/10.1016/j.margeo.2007.04.006>
- Godt, J.W., Baum, R.L., Lu, N., 2009. Landsliding in partially saturated materials. *Geophys. Res. Lett.* 36, 1–6. <https://doi.org/10.1029/2008GL035996>
- Heiss, J.W., Puleo, J.A., Ullman, W.J., Michael, H.A., 2015. Coupled surface-subsurface hydrologic measurements reveal infiltration, recharge, and discharge dynamics across the swash zone of a sandy beach 8834–8853. <https://doi.org/10.1002/2015WR017200.A>
- Holtz, R.D., Kovacs, W.D., 1981. *An Introduction to Geotechnical Engineering*, An Introduction to Geotechnical Engineering. Englewood Cliffs, New Jersey.
- Horn, D.P., Baldock, T.E., Li, L., 2007. The Influence of Groundwater on Profile Evolution of Fine and Coarse Sand Beaches.
- Krahn, J., Fredlund, D.G., 1971. On total, matric and osmotic suction.pdf. *Soil Sci.*
- Mory, M., Michallet, H., Bonjean, D., Piedra-Cueva, I., Barnoud, J.M., Foray, P., Abadie, S., Breul, P., 2007. A field study of momentary liquefaction caused by waves around a coastal structure. *J. Waterw. Port, Coast. Ocean Eng.* 133, 28–38.

- [https://doi.org/10.1061/\(ASCE\)0733-950X\(2007\)133:1\(28\)](https://doi.org/10.1061/(ASCE)0733-950X(2007)133:1(28))
- O'Dea, A., Brodie, K.L., Hartzell, P., 2019. Continuous Coastal Monitoring with an Automated Terrestrial Lidar Scanner. *J. Mar. Sci. Eng.* 7, 37.
<https://doi.org/10.3390/jmse7020037>
- Palmsten, M.L., Holman, R.A., 2011. Infiltration and instability in dune erosion. *J. Geophys. Res. Ocean.* 116, 1–18. <https://doi.org/10.1029/2011JC007083>
- Qi, W.G., Gao, F.P., 2018. Wave induced instantaneously-liquefied soil depth in a non-cohesive seabed. *Ocean Eng.* 153, 412–423.
<https://doi.org/10.1016/j.oceaneng.2018.01.107>
- Sallenger, A.H.J., 2000. Storm impact scale for barrier islands. *J. Coast. Res.* 16, 890–895.
- Seymour, R., Guza, R.T., O'Reilly, W., Elgar, S., 2005. Rapid erosion of a small southern California beach fill. *Coast. Eng.* 52, 151–158.
<https://doi.org/10.1016/j.coastaleng.2004.10.003>
- Sherman, D.J., Nordstrom, K.F., 1985. Beach scarps. *Ann. Geomorphol.* 29, 139–152.
- Stockdon, H.F., Holman, R.A., Howd, P.A., Sallenger, A.H., 2006. Empirical parameterization of setup, swash, and runup. *Coast. Eng.* 53, 573–588.
<https://doi.org/10.1016/j.coastaleng.2005.12.005>
- Tonkin, S., Yeh, H., Kato, F., Sato, S., 2003. Tsunami scour around a cylinder. *J. Fluid Mech.* 496, 165–192. <https://doi.org/10.1017/S0022112003006402>
- Turner, I.L., Masselink, G., 1998. Swash infiltration-exfiltration and sediment transport. *J. Geophys. Res.* 103, 30813–30824.
- van Bemmelen, C.W.T., de Schipper, M.A., Darnall, J., Aarninkhof, S.G.J., 2020. Beach scarp dynamics at nourished beaches. *Coast. Eng.* 160, 103725.
<https://doi.org/10.1016/j.coastaleng.2020.103725>
- van Rijn, L.C., Tonnon, P.K., Sánchez-Arcilla, A., Cáceres, I., Grüne, J., 2011. Scaling laws for beach and dune erosion processes. *Coast. Eng.* 58, 623–636.
<https://doi.org/10.1016/j.coastaleng.2011.01.008>
- Yeh, H., Mason, H.B., 2014. Sediment response to tsunami loading: Mechanisms and estimates. *Geotechnique* 64, 131–143. <https://doi.org/10.1680/geot.13.P.033>

Appendix A: Geotechnical Testing

Proctor Compaction Test

We carried out the Modified Proctor Compaction test to understand the compaction potential of the dune sand at different water contents, and to determine the optimum water content and maximum dry density of the sand. Testing was carried out according to ASTM D1557, summarized below.

We first oven-dried the sand and sieved it with a coarse mesh to remove plants and rocks. We tested the sand at a number of water contents by incrementally adding water to the sand and testing it. We compacted the sand using the standard compaction weight in the compaction mold specified by the ASTM standard. The number of lifts, height of lifts, and blow pattern is also detailed in the ASTM standard. After the sand was compacted in the mold, we removed the collar and trimmed the sample.

For each sample, we recorded the weight of the wet sand and mold, then removed a small sand sample to test the water content. The water content, the weight of the wet sand, and the volume of the mold were used to calculate the dry density for samples at each water content. Figure 1 shows the results from this test; the cluster of points at low water contents is because during the first day of testing, we misjudged the amount of water necessary to cover the full range of water contents needed for the test.

The optimum water content for this sand is approximately 16%, and the maximum dry density is 16.5 kg/m^3 .

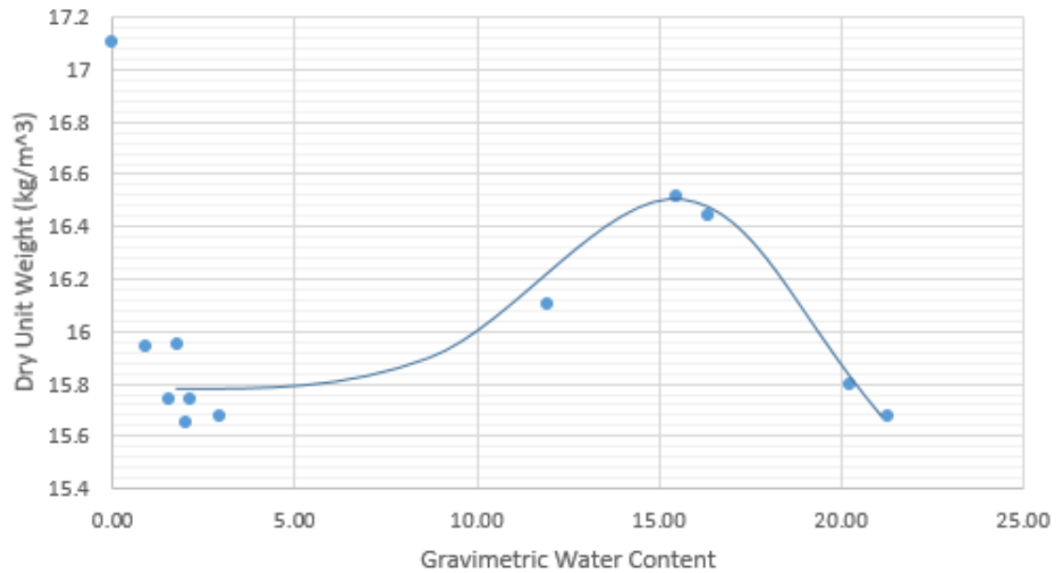


Figure 1: Results from Modified Proctor Compaction Test

Minimum and maximum index density

Minimum and maximum index density tests (ASTM D4254 and ASTM D4253, respectively) were also carried out on the sand. The minimum index density test involves using a funnel to place sand into a mold, then weighing the sand in the mold. The maximum index density test involves compressing the sand using a vibratory table and a weight placed on top of the sand, then trimming the sample and weighing the sand in the mold. Details on the test specifications are given in their respective ASTM standards. The minimum index density of the sand is 14.7 kN/m^3 and the maximum index density of the sand is 16.1 kN/m^3 .

Grain Size Distribution

A grain size distribution test was carried out in accordance with ASTM D6913. Results from 3 trials are presented below in Figure 2.

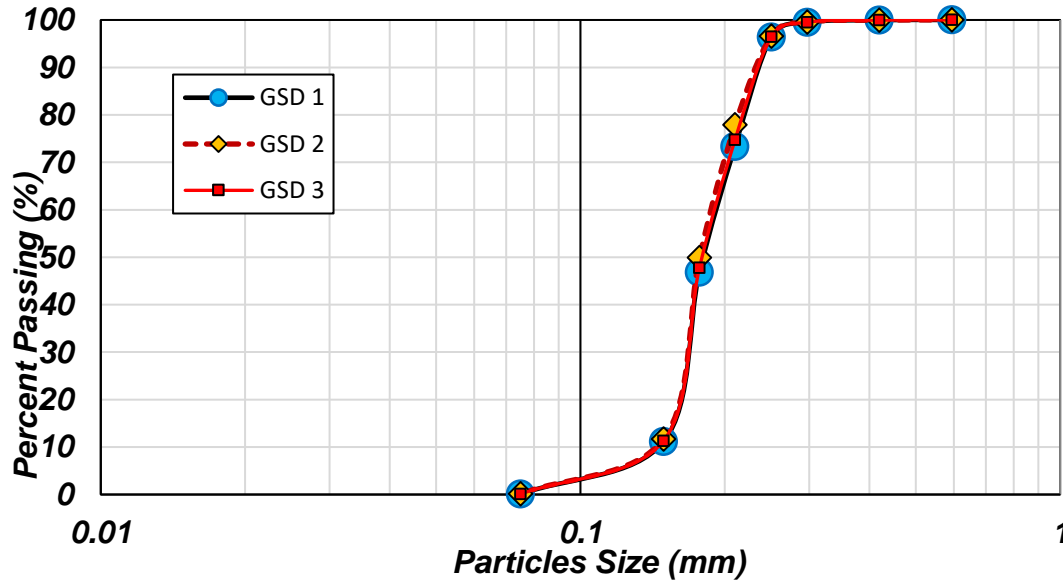


Figure 4: Results from grain size distribution test, courtesy of Pegah Ghasemi

Dynamic Cone Penetrometer and Nuclear Densitometer

We used a dynamic cone penetrometer (DCP) for several kinds of testing on sand compaction. First, we did field testing on the coast to get a benchmark for the compaction of natural dunes. We tested the dunes in areas where the dunes were vegetated and bare, and in one of the bare dune areas, had the chance to test the sand after 4 feet of sand and 7 feet of sand had been removed. Figure 2 shows the DCP results from the field testing. The x-axis shows the number of inches per blow of the DCP, and the y axis shows the distance below the sand surface. Dashed lines represent vegetated areas of the dune, and solid lines represent bare areas of the dune. Areas 5 and 6 had sand removed from the upper 4 and 7 feet, respectively, before testing.

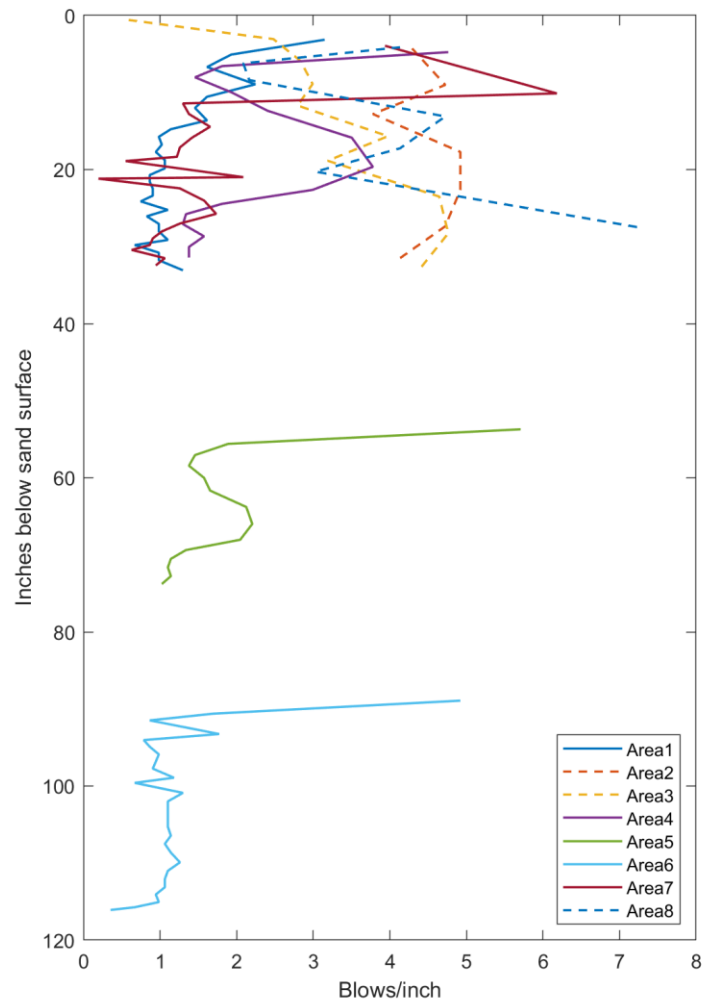


Figure 3: Results from dynamic cone penetrometer field testing.

We also used the DCP to look at the effect of our vibrating plate compactor on the sand. To do this, we built a test section with 4 lifts of 1 ft each. We separated this test section into 6 sections and compacted each with a different number of compactor passes. We then tested each section with the DCP and a nuclear densitometer to correlate the dry density of the sand with the DCP results. The DCP results are presented in Figure 3 (same setup as previous figure).. It should be noted that the DCP results in upper layer of sand do not appear to be consistent with the compaction of the soil in the remaining depth. The nuclear densitometer only measures the density of approximately the top 12 in of soil, therefore we believe the nuclear densitometer results do not necessarily represent the overall compaction in each section. We saw minimal change with increasing compactive effort, and, for the dune, decided on a compaction scheme in which the number of compaction passes for each lift decreased with each lift added, beginning with 5 passes at the base and reducing to 1 at the dune surface.

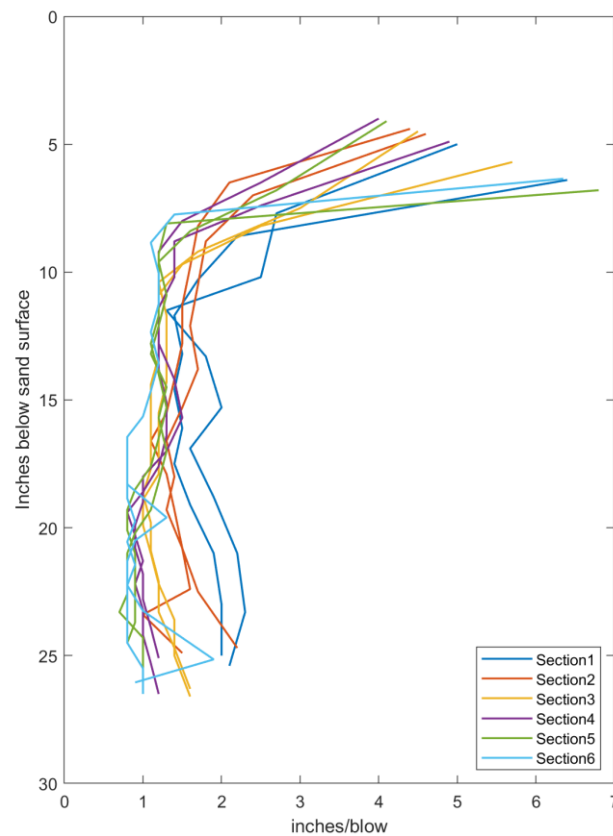


Figure 4: Results from Dynamic Cone Penetrometer test section testing

After construction of the dune, we used the DCP to measure the compaction at several cross shore locations along the dune. Two DCP trials were completed at each cross shore location, and the results are presented below.

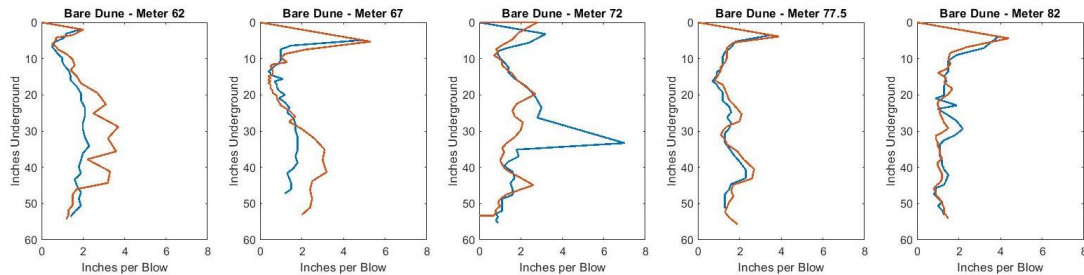


Figure 5: Results from Dynamic Cone Penetrometer testing on the bare dune

Moisture Sensor Calibration

To calibrate moisture sensors, we tested 15 sensors in three groups of five in a modified proctor compaction mold. The mold was chosen for its convenient size. For every group, we tested 6 water contents ranging from air-dry to a water content of 0.25 (the maximum water content possible before the mold began leaking). Each sensor was buried below the surface of the sand so that the collection volume (detailed in the manufacturer’s datasheet) did not touch the sides of the mold or surface of the sand. Each sensor was buried and reburied twice, and the voltage readings from each burial were averaged. After the third sensor of 5 in the group, a small sample of sand was removed to test the water content. After all the sensors in the group were tested at a single water content, the sand was removed, water was added, and the process was repeated.

The gravimetric water content determined during the test was converted to the volumetric water content using the bulk density calculated from the air-dry sample. After the data for 3 sensor groups was collected, a cubic polynomial was fit to the data collected from each sensor, as suggested by the manufacturer. Data and calculations are collected in Excel sheets titled “Moisture Sensors Calibration.xlsx” and “calibrationcalcs.xlsx”

When plotting the calibration curves, it became evident that the shape of the calibration curve was affected by the water contents tested during the calibration. Figure 6 shows all the sensor groups.

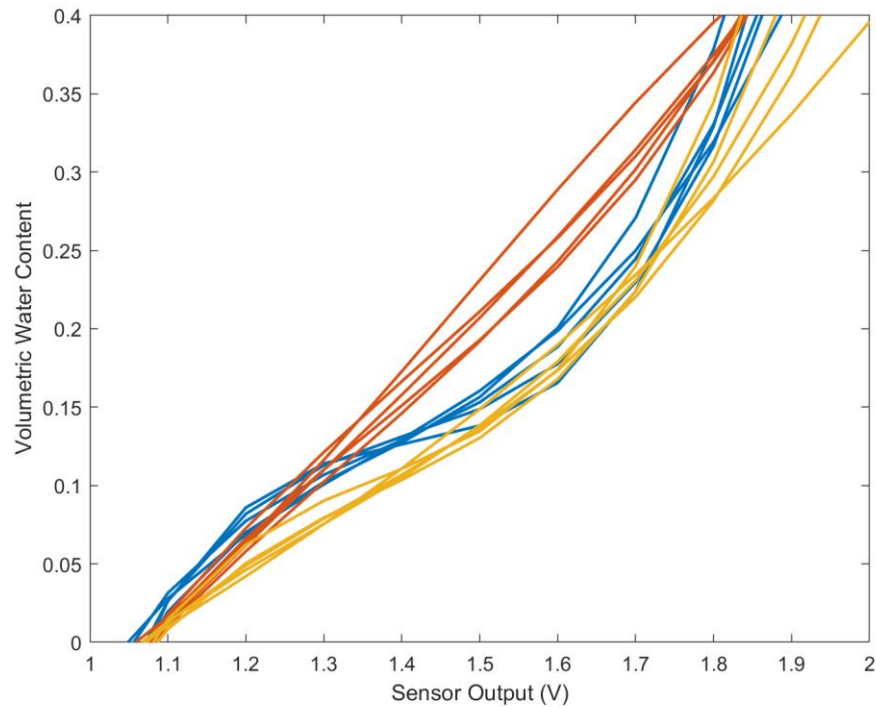


Figure 6: Moisture sensor calibration curves for all sensors tested

Each group of calibration curves has a distinctly different shape, which led us to infer that the differences between individual sensor calibrations were caused mainly by the differences in the water contents used for calibration. We decided to average the calibration curves and use the same curve for all sensors. Figure 7 shows the individual sensor calibration curves (grey) overlaid with the averaged curve (red).

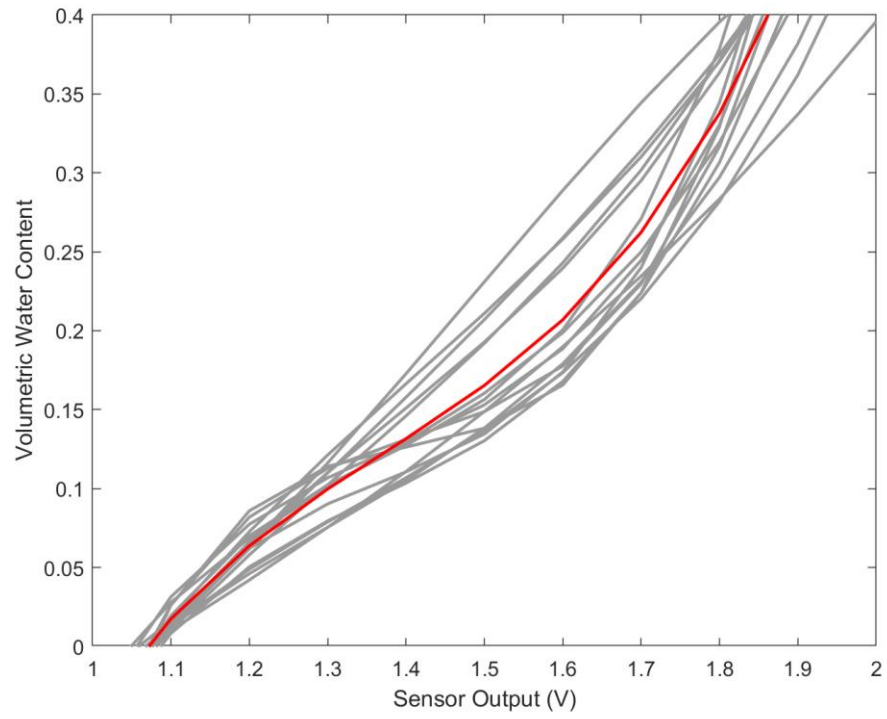


Figure 7: Moisture sensor calibration curves for all sensors tested (grey) and averaged curve (red)

Appendix B: Lidar Processing

Lidar Rectification Procedure

Step 1: Set up baseline

The baseline scan is developed from two scans taken prior to the first trial of the vegetated dune without moving the lidar between them. Scan #1 is low resolution, but captures a large view of the wave lab, including wave lab reflectors. Scan #2 is higher resolution, but only captures the flume. We used a combination of permanent wave lab reflectors and temporary reflectors installed for this experiment in Scan #1 to calculate a transformation matrix for the baseline scan. This transformation matrix was then applied to Scan #2 to rotate it so it could be used as the baseline scan for plane matching.

Scan # 1 filename: '20190621_DAQ001_VD_h202_H020_T1p53 - SINGLESCANS - 20190621_DAQ001_VD_h202_H020_T1p53 - Scan001.txt')

Scan # 2 filename: '20190621_DAQ001_VD_h202_H020_T1p53 - frame.txt'

The transformation matrix from Scan # 1 was calculated using a matlab script to identify reflectors within the scan after a rough rotation (matrix generated manually in cloudcompare) and minimize the least squares difference to the surveyed locations of the sensors. Note: due to the low resolution of Scan #1, the general method of finding the reflectors using the top 3.5% of reflectance values didn't give accurate results. Instead, intensity values over 5000 were considered to be part of the reflector, all other points were discarded.

Matlab scripts used: baselinerotation.m, findReflectors.m, transformationparameters.m, Rigid3DTransform_GLS.m, trimDataRegions.m

Reflectors used to rectify baseline scan:

Reflector	X	Y	Z
LWF01	102.626	10.506	10.059
LWF02	79.992	15.563	8.917
LWF03	64.761	15.545	8.878
LWF16	102.637	-7.763	10.058
DUNE01	96.561	-1.817	5.278
DUNE02	96.564	1.821	5.287

Final Baseline Transformation Matrix:

$$FinalT = \begin{bmatrix} -0.8618 & -0.0046 & 0.5064 & 51.3257 \\ 0.0036 & -1.0000 & -0.0031 & -0.6489 \\ 0.5064 & -0.0008 & 0.8618 & 6.6734 \\ 0 & 0 & 0 & 1 \end{bmatrix}$$

* note: more exact values are saved in matlab file

FinalBaseLineTransformationMatrix.mat

Step 2: Plane Rectification:

The plane rectification method uses 10 planes oriented in different directions around the scanner to match each frame scan to the baseline scan in a way that minimizes the least square errors and generates the corresponding transformation matrix.

First the scan needing registration is loaded from the 'Lidar>frame' folder. It will undergo 3 transformations. Transformation #1 (Rough Transformation) uses a fixed matrix generated manually from cloudcompare, and is the same for every scan. Transformation #2 (Fine Transformation) does a least-squares fit by finding the 3 reflectors used in each scan and fitting them to their surveyed locations to get the scans lined up as well as possible so the correct planes are selected in the plane transformation. Transformation #3 (Plane Transformation) uses the 10 planes mentioned above to fit the scan to the same 10 planes in the baseline.

Rough Transformation: Uses a fixed rotation matrix generated manually in CloudCompare to rotate scan. This is done so the reflector-finding code will look in the correct place for reflectors. The rotation matrix changes when the lidar is moved forward.

Fine Transformation: Using the reflector-finding code, three reflectors are identified in the scan. Using their surveyed locations, a rotation matrix is generated to minimize the least squares error, and the scan is rotated. This transformation is intended to rectify the scan as closely to the baseline as possible. However, due to the limited number of reflectors and the fact that the reflectors visible in the scans changed when the lidar moved forward, this rectification wasn't close enough. However, it aided in getting the scans lined up so the plane-matching algorithm worked well.

Plane Transformation: The plane transformation matches 10 planes at different locations along the flume wall in the baseline and the scan previously rotated using the reflectors. The plane-matching code trims the baseline scan and scan to be rotated into boxes given by the *planes.mat* file, which gives the dimensions and centroid of trimming boxes. The only points remaining in this box should be on the selected planes. Then, 100 points are sampled at random from the points in the box, and a least squares fit is used to match them to the corresponding plane. Below is an image showing the location of the planes (in light blue) within the scan.

Note that reflectors are NOT used to calculate the transformation matrix. They are only used to line up the scans so that the plane-selection algorithm can correctly select planes.

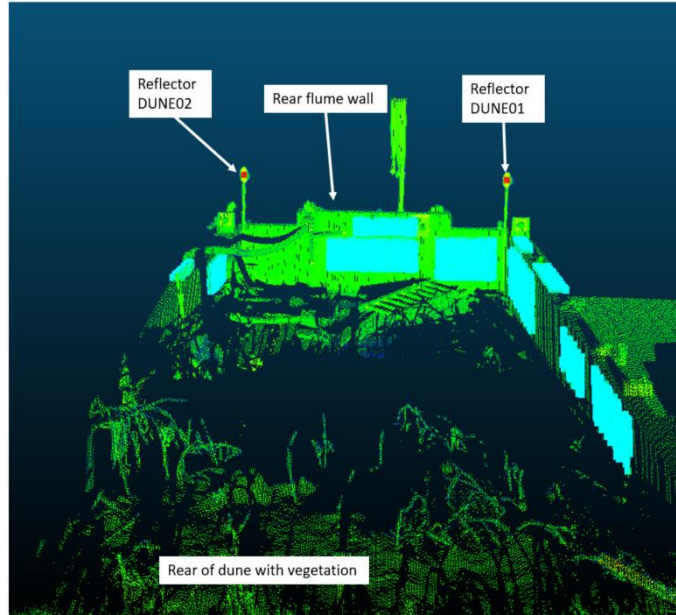


Figure 1: Example of lidar frame scan with matching planes

Rotation and translation matrices are generated for each of these rotations. After all three transformations, the following is used to generate the final transformation matrix for the frame and line scans for a particular trial.

$$\begin{aligned}
 RR_{final} &= RR_{plane} * RR_{fine} * RR_{rough} & (3x3) \\
 T_{final} &= T_{plane} + T_{fine} + T_{rough} & (3x1) \\
 M_{final} &= \begin{bmatrix} RR_{final} & T_{final} \\ [0 \ 0 \ 0] & 1 \end{bmatrix} & (4x4)
 \end{aligned}$$

Matlab files used: lidarplanecoregfinal.m, rotatelidar.m, findAndTrimPlaneRegions.m, SolvePlanes.m, AtanAzimuth.m, RT2transformationMatrix.m, PropRangeEncoder.m, SolvePlanes.m, Rigid3DTransform.m, ThinPlanes.m, unrotateXYZ.m, planes.mat, params_final.mat, trimDataRegions.m, findAndTrimPlaneRegions.m

Lidar Processing

After the rotation matrix for each trial is determined, the linescans can be processed. First, the linescans need to be converted from a continuous stream of points to a structure with separated lines. As the lidar scanned the dune by scanning from approximately 50 deg to

120 deg and then resetting back to 50 deg, a new line is identified when the change in angle between two consecutive points is greater than 60. In the raw lidar data, the timestamp is recorded as an internal lidar time, which is a large number without any known physical significance. The timestamp of the first line is subtracted from the rest to create a time vector starting from 0 at the first line. Additionally, the internal lidar time resets itself periodically, which is accounted for in the processing code. After the linescans are separated, each line is gridded onto the one of two 0.5 cm grids. The first grid spans from meter 55-85, and the second from 65-85, due to the lidar moving forward in the last trials of the experiment.

Matlab files used: lidarlinescanprocessing.m, importlidar.m, rotatelidar.m, separatelines.m

Once the linescan is separated into lines and gridded, the linescans can be processed to present more useful information. First, the sand surface is identified using a 50 point (25 second) moving minimum filter in time. This identifies the sand surface, which is the lowest possible point that can be recorded at any location. The sand surface is then filtered with a standard deviation filter to remove outliers.

After the sand surface is identified, it is subtracted from the original linescan data, leaving only the water elevation above the sand, or the swash depth. The runup extent for the first time step is identified using the cross-shore location where the swash depth is less than 2 cm. After the first time step, the code looks for the swash depth threshold within a spatial window of 4 meters centered on the previous runup location.

The output of this operation is a structure called 'runup' with the following fields:

- **Zminimum:** the sand surface. Number of rows matches with number of x grid coordinates, number of columns matches with number of time steps.
- **Z:** rotated linescan data presented in a matrix with the same setup as Zminimum.
- **ZNfiltered:** the swash depth. Setup is the same as Zminimum matrix.
- **Runup:** a 3-column matrix. The first column is the x-coordinate of runup, the second column is the z-coordinate of runup, and the third column is the timestep.
- **x:** x vector, for use in plotting matrices.

Fixing Time Vector

Due to limitations of the lidar timing system, the only recorded start time was when the operator began data collection. However, the lidar mirror took time to initialize, and thus started collecting data after the recorded start time. To determine this temporal offset, we used the data from the overhead cameras with a known start time collected during the experiment and extracted the runup pattern using a similar procedure as the lidar. With the camera data, we used a change in pixel brightness rather than a threshold swash depth to identify the runup extent. We then cross correlated the camera-extracted runup with the runup calculated from the lidar data to identify the time offset between the two signals. Figure 2 shows an example of the runup signal determined from the dune-view camera (Figure 2a), the berm-view camera (Figure 2b), and the lidar (Figure 2c) prior to the time lag adjustment. For the trials with a significant cross-correlation, the time lag calculated for that trial was used. Not all trials had a significant cross-correlation value; some were missing video data or the runup extent wasn't captured by either camera. For these trials, the average of the time lag of the other trials was used.

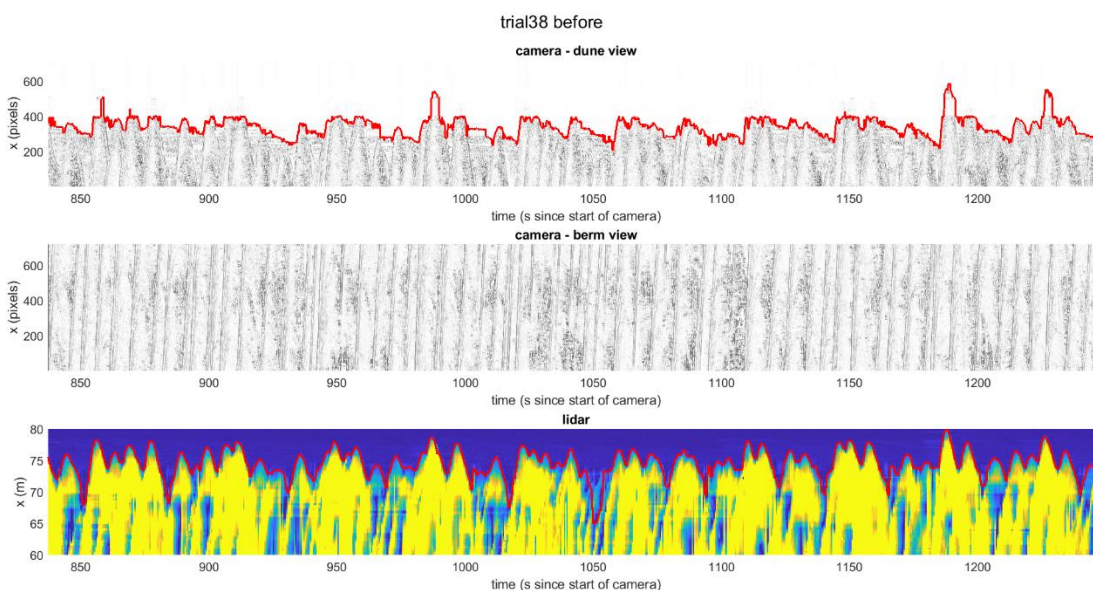


Figure 2: Data used to identify lidar time lag: (a) runup derived from dune-view camera, (b) runup derived from berm-view camera, (c) runup derived from lidar

Appendix C: Forcing Conditions

To decide the ideal forcing conditions for our experiment, we looked at a number of storms from around the United States. Initially, we hoped to create a “typical” hurricane based on averaging data from a number of historical hurricanes. However, it became clear that storms had a large variation in the duration and intensity of the storm surge. Figure 1 shows a time series of the storm surge during Hurricane Harvey, which made landfall near Port Aransas, Texas. The x-axis represents the number of days since the beginning of the hurricane year, and the y-axis represents the elevation of the recorded water level above the expected tide. The red dots mark the beginning and end of the storm surge. The storm surge is characterized by an abrupt increase in water level followed by a sudden decrease. Data from all the following storms was based on the NOAA tides and currents stations.

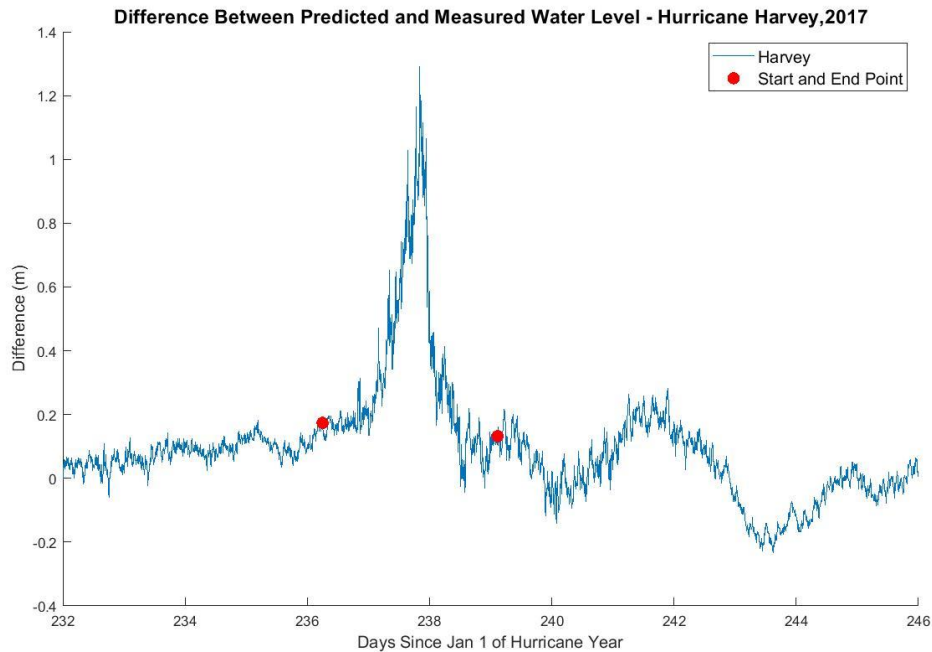


Figure 1: Hurricane Harvey storm surge

In contrast, Figure 2 shows the storm surge during Hurricane Joaquin, which caused elevated water levels along the Atlantic coast. The data in Figure 2 was collected in Duck, North

Carolina. The storm created a storm surge with a slightly lower rate of increase, and the water level was elevated for much longer than in Hurricane Harvey.

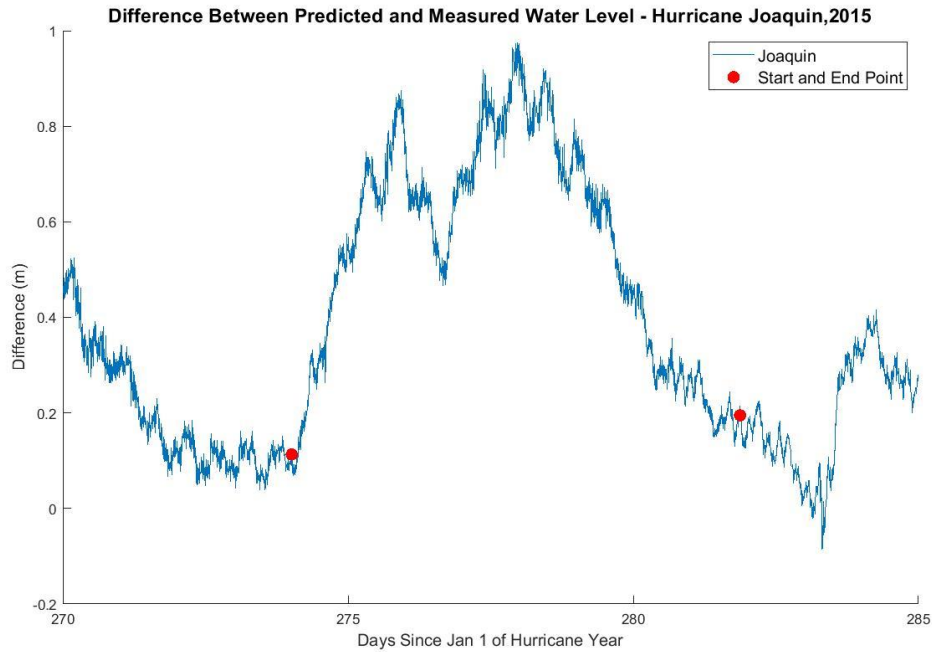


Figure 2: Hurricane Joaquin storm surge

Hurricane Michael (Figure 3) has yet another shape. The storm surge slowly ramps up over a number of days, then quickly decreases.

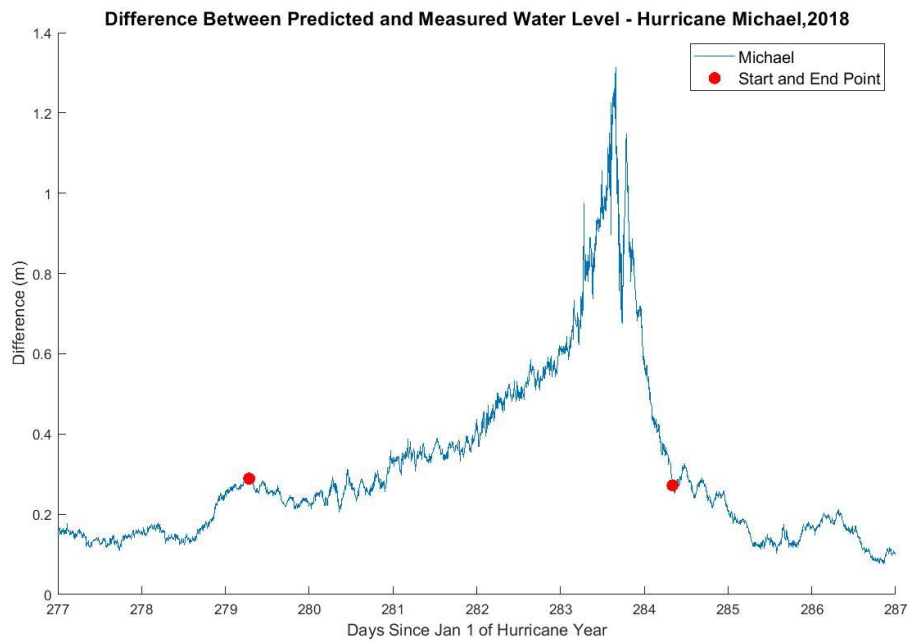


Figure 3: Hurricane Michael storm surge

Based on these and other examples of storm surges in the United States, it was difficult to identify a consistent pattern in the increase in water level during hurricanes. The storm surge patterns also appeared to vary regionally, with steep spikes in water level occurring on the Texas coast and longer duration storm surge events occurring on the Central and North Atlantic Coasts. Rather than try and create a single storm representative of a “typical” hurricane, we decided to use data from a single storm to force our experiment. Because our dune profile was from New Jersey and because we wanted to ramp up erosion more slowly than some of the steeper storms, we chose to use Hurricane Sandy as our model storm. Figure 4 shows the storm surge data from the hurricane.

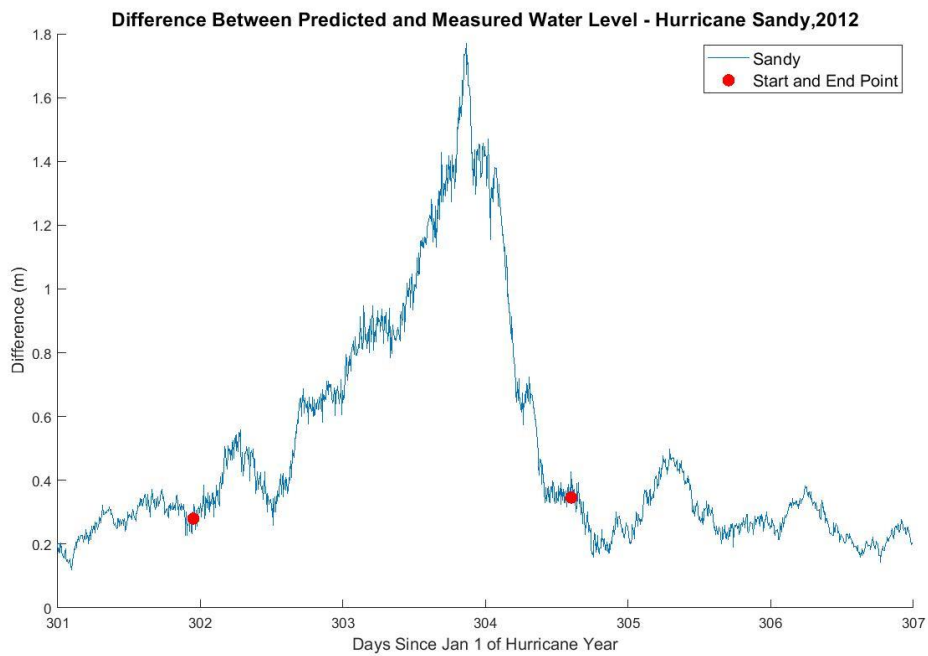


Figure 4: Hurricane Sandy storm surge